Anomalous Josephson current through a driven double quantum dot

Carlos Ortega-Taberner,[1,2] Antti-Pekka Jauho,[3] and Jens Paaske[4]
[1]*Department of Physics, Stockholm University, AlbaNova University Center, SE-106 91 Stockholm, Sweden*
[2]*Nordita, KTH Royal Institute of Technology and Stockholm University, SE-106 91 Stockholm, Sweden*
[3]*Center for Nanostructured Graphene, Department of Physics, Technical University of Denmark, DK-2800 Kongens Lyngby, Denmark*
[4]*Center for Quantum Devices, Niels Bohr Institute, University of Copenhagen, DK-2100 Copenhagen Ø, Denmark*

(Received 14 July 2022; revised 31 January 2023; accepted 28 February 2023; published 29 March 2023)

Josephson junctions based on quantum dots offer a convenient tunability by means of local gates. Here we analyze a Josephson junction based on a serial double quantum dot in which the two dots are individually gated by phase-shifted microwave tones of equal frequency. We calculate the time-averaged current across the junction and determine how the phase shift between the drives modifies the current-phase relation of the junction. Breaking particle-hole symmetry on the dots is found to give rise to a finite average anomalous Josephson current with phase bias between the superconductors fixed to zero. This microwave gated weak link thus realizes a tunable "Floquet φ_0 junction" with maximum critical current achieved for driving frequencies slightly off resonance with the subgap excitation energy. We provide numerical results supported by an analytical analysis for infinite superconducting gap and weak interdot coupling. We identify an interaction-driven 0-π transition of anomalous Josephson current as a function of driving phase difference. Finally, we show that this junction can be tuned so as to provide for complete rectification of the time-averaged Josephson current-phase relation.

DOI: 10.1103/PhysRevB.107.115165

I. INTRODUCTION

The Josephson junction (JJ) has become a ubiquitous device serving in a wide range of applications, including the superconducting qubits which have led to impressive advances in quantum computing during the past two decades [1–5]. The weak link coupling the two superconductors can either be a plain insulating tunnel barrier, or it may exhibit internal structure such as a normal region, a quantum point contact, a magnetic tunnel barrier, or a quantum dot (QD), which all host subgap states which may strongly influence the current-phase relation (CPR) of the junction [6–12]. In this way, electrically gatable links such as quantum dots or semiconductors offer a certain tunability of the JJ characteristics [13–16], a feature which has been employed in the design of a hybrid gatemon [17–19], adding gate control to the superconducting transmon qubit [20,21], which has already demonstrated its efficiency in solid state quantum computing [22–24].

Whereas normal Josephson junctions carry no current at zero phase bias, $\varphi_{sc} = \varphi_L - \varphi_R$, a weak link which breaks both time-reversal and chiral symmetry may carry an anomalous Josephson current between two superconductors maintained at zero phase bias [25]. A number of proposals [25–38] have been made for such φ_0 junctions with an anomalous Josephson current, $I(\varphi_{sc}) = I_C \sin(\varphi_{sc} + \varphi_0)$, at least two of which have already been realized experimentally [39,40]. Of particular relevance to the present work is the proposal by Zazunov *et al.* [25] to use a multiorbital QD with interorbital (spin-orbit) tunneling and an external field. With such a link in the JJ, traversing electrons pick up different phases, depending on the tunneling direction, giving rise to an anomalous Josephson current. This proposal has since been realized in an experiment by Szombati *et al.* [40], using an InSb-wire QD contacted by superconducting NbTiN leads. Here, we propose a nonequilibrium version of the multiorbital QD considered in Ref. [25], based on the device illustrated in Fig. 1. In this Josephson junction, the two superconductors are coupled by a serial double quantum dot (DQD) where the two dots are driven by individual ac gate voltages with a common

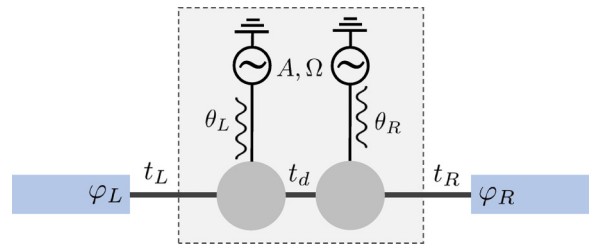

FIG. 1. Sketch of a Josephson junction with a structured weak link (gray region) based on a driven double quantum dot. The superconductors (blue) are maintained at a fixed phase bias $\varphi_{sc} = \varphi_L - \varphi_R$, and the weak link is driven by two microwave gates with the same amplitude and frequency, A, Ω, shifted in phase by $\theta_d = \theta_L - \theta_R$. The internal and the two external tunneling amplitudes are denoted by t_d, t_L, and t_R, respectively.

amplitude, A, and microwave frequency, Ω. This endows each of the QDs with Floquet sidebands, which play the roles of the additional spin-orbit coupled orbitals in Ref. [25]. As we demonstrate below, the phase difference between the two drive voltages, $\theta_d = \theta_L - \theta_R$, can have a strong influence on the time-averaged JJ CPR, and with QD levels tuned away from particle-hole symmetry it gives rise to anomalous current, which in the limit of weak tunnel couplings reduces to a simple φ_0 junction, with $\varphi_0 = \theta_d$. Since the time-averaged critical current is maximized when the microwave frequency is close to the energy for exciting both of the subgap states induced in the two proximitized quantum dots, this device comprises a nonadiabatic Cooper pair pump, or more aptly a "Floquet φ_0 junction."

The undriven DQD Josephson junction with individual gating of the two dots has already been realized experimentally [16,41–43], and understood to constitute a strongly correlated transport problem involving the formation of subgap states, which depend strongly on the charge configuration of the (Coulomb blockaded) dots [12,16,32,44–49]. Here we circumvent a number of these complications by replacing each of the dots with a noninteracting resonant level. Whereas this would clearly be a poor description of Coulomb blockaded QDs in many other respects, the two models do share the crucial features of the mechanism we wish to illustrate, namely, the presence of subgap states with a strong gate dependence.

As a weak link for a JJ, the resonant level model behaves much like a quantum point contact (QPC) with a CPR which reflects the phase dispersion of the subgap Andreev bound states (ABS) [8,44,50]. A JJ based on a Coulomb blockaded QD, however, is known to exhibit a transition from a $\varphi_0 = \pi$ to a $\varphi_0 = 0$ phase [9,10,12,14,47,48], and the results presented below are therefore of greater direct relevance for a realistic Coulomb blockaded QD in its $\varphi_0 = 0$ phase stabilized for strong tunnel couplings [51], or for a long normal junction with a finite dwell time [52]. Nevertheless, the effects discussed here rely merely on the breaking of time-reversal and chiral symmetry by the phase-shifted drives, and should apply quite generally to the fully interacting system. This is confirmed for the interacting infinite-gap limit, considered in the Appendix.

Dating back to the seminal work on photon-assisted tunneling by Tien and Gordon [53], the problem of nonadiabatically (microwave) driven Josephson junctions has been expanded to include also junctions with QPC, QD, DQD, or magnetic adatom weak links [54–63]. Experimentally, the ABS in such junctions have been measured and manipulated using microwave spectroscopy [64–69], and these techniques are by now becoming widely available. Recently, Venitucci *et al.* [61] demonstrated that phase-shifted microwave voltages applied to each of the superconductors in a JJ with a single resonant level as the weak link can give rise to photon-assisted Cooper pair transfer and a tunable φ_0 junction. Similarly, Soori and Sivakumar [70] have studied a finite-size tight-binding model of a superconductor/normal conductor/superconductor (SNS) junction and found that a phase-shifted drive on the two sites comprising their normal region leads to anomalous Josephson current. The model studied here is similar in spirit but not equivalent to these two studies.

We consider the driven DQD itself as a highly tunable weak link and map out its time-averaged anomalous CPR. This reveals a highly nontrivial dependence on the time average as well as the phase shift of the two oscillating gate voltages, including a complete rectification of the time-averaged Josephson current. We employ the infinite-gap limit to understand the detailed weak-coupling behavior near resonant driving, including a closed analytical expression for the φ_0 phase shift. We also use a numerically exact Floquet solution in the infinite-gap limit to establish the symmetries of the time-dependent Josephson current, to explore the effects of interactions, and to assess the sensitivity to initial conditions which are conveniently circumvented in the steady-state Green's functions approach.

The paper is organized as follows. In Sec. II we present the model. In Sec. III we define the relevant Nambu-Floquet-Keldysh Green's functions and provide an expression for the time-averaged steady-state current to be calculated. In Sec. IV we study the limit of infinite gap, in which the main effect of the φ_0 junction can be established analytically in the limit of weak interdot tunnel coupling. Section V contains the numerical results for the current and the CPR for the driven junction. Section VI briefly summarizes the main conclusions. The Appendix provides a supplementary analysis for the infinite-gap limit using Floquet theory, which allows us to also investigate the effects of local Coulomb interactions, and to confirm the rectification of the time-averaged supercurrent.

II. MODEL

We consider a noninteracting serial double quantum dot with on-site energies modulated by individual ac gate voltages and tunnel coupled to two (left/right) superconducting leads (cf. Fig. 1). The Hamiltonian reads

$$H(t) = \sum_{\alpha=L,R} H_{sc,\alpha} + H_{\rm d}(t) + H_{\rm t}, \tag{1}$$

with superconducting leads described by BCS Hamiltonians

$$H_{sc,\alpha} = \sum_{\mathbf{k},\sigma} [\xi_{\alpha\mathbf{k}} c^\dagger_{\alpha\mathbf{k}\sigma} c_{\alpha\mathbf{k}\sigma} + (\Delta e^{i\varphi_\alpha} c_{\alpha\mathbf{k}\uparrow} c_{\alpha-\mathbf{k}\downarrow} + \text{H.c.})], \tag{2}$$

for $\alpha = L, R$. The two leads are kept at the same chemical potential and are assumed to have the same gap magnitude, $\Delta > 0$, with different phases, $\varphi_{L,R} = \pm\varphi_{sc}/2$. Both leads are represented by a featureless band structure near a common chemical potential, i.e., $\xi_{\alpha\mathbf{k}} = \varepsilon_{\alpha\mathbf{k}} - \mu$, corresponding to a common density of states, ν_F, near the Fermi level. The time-dependent Hamiltonian of the double quantum dot system reads

$$H_{\rm d}(t) = \sum_{\sigma;\alpha,\alpha'\in L,R} d^\dagger_{\alpha\sigma} \left[\varepsilon_{d\alpha}(t)\tau^0_{\alpha\alpha'} + t_d \tau^x_{\alpha\alpha'}\right] d_{\alpha'\sigma}, \tag{3}$$

with individual ac gate voltages given as $\varepsilon_{d\alpha}(t) = \varepsilon_d + A\cos(\Omega t + \theta_\alpha)$, in terms of common (time) average energies, ε_d, driving amplitudes, A, frequencies, Ω, and two independent phase constants, θ_α. Here, τ^i denotes the ith Pauli matrix, τ^0 the Kronecker delta, and t_d is the interdot tunneling

amplitude. The tunneling Hamiltonian reads

$$H_{\rm t} = \sum_{\mathbf{k},\sigma,\alpha=L,R} t_\alpha c^\dagger_{\alpha\mathbf{k}\sigma} d_{\alpha\sigma} + \text{H.c.} \tag{4}$$

Written in terms of Nambu spinors, $\psi^\dagger_{\alpha\mathbf{k}} = (c^\dagger_{\alpha\mathbf{k}\uparrow}, c_{\alpha-\mathbf{k}\downarrow})$ and $\phi^\dagger_\alpha = (d^\dagger_{\alpha\uparrow}, d_{\alpha\downarrow})$, the full Hamiltonian reads

$$\begin{aligned} H(t) = &\sum_{\alpha\mathbf{k}} \psi^\dagger_{\alpha\mathbf{k}}(\xi_{\alpha\mathbf{k}}\sigma_z - \Delta\sigma_x)\psi_{\alpha\mathbf{k}} \\ &+ \sum_{\alpha\alpha'} \phi^\dagger_\alpha\big(\varepsilon_{d\alpha}(t)\tau^0_{\alpha\alpha'} + t_d\tau^x_{\alpha\alpha'}\big)\sigma_z\phi_{\alpha'} \\ &+ \sum_{\alpha\mathbf{k}} (\psi^\dagger_{\alpha\mathbf{k}}\mathcal{T}_\alpha\phi_\alpha + \phi^\dagger_\alpha\mathcal{T}^*_\alpha\psi_{\alpha\mathbf{k}}), \end{aligned} \tag{5}$$

where the phase of the superconducting leads has been gauged into the tunneling matrix, $\mathcal{T}_\alpha = t_\alpha\sigma_z e^{i\sigma_z\varphi_\alpha/2}$. For simplicity, we assume below that tunneling amplitudes to the leads are real and equal, i.e., $t_L = t_R \equiv t$.

As discussed in the Introduction, we neglect the charging energies of both quantum dots, except for the limiting case of infinite gap considered in the Appendix, and consider this noninteracting resonant level model as an effective model for a proximitized quantum dot.

III. KELDYSH FLOQUET GREEN'S FUNCTIONS

To calculate the current through the ac-driven device, we employ the nonequilibrium Green's function technique [71–73]. Dealing with a harmonic drive, it is convenient to use Floquet-Keldysh Green's functions [74,75], which offer a representation of the two-time Green's functions, which, besides being convenient for numerical calculations, allows for some degree of physical interpretation of the elementary transport process in terms of Floquet sidebands. The time-dependent charge current from dot α to lead α for this driven junction is found as [73]

$$\begin{aligned} I_\alpha(t) = 2(-e)\text{Tr}\Bigg\{\sigma_z\text{Re}\Bigg[\int dt'\,\big(&G^R_{d,\alpha\alpha}(t,t')\Sigma^<_\alpha(t',t) \\ &+ G^<_{d,\alpha\alpha}(t,t')\Sigma^A_\alpha(t',t)\big)\Bigg]\Bigg\}, \end{aligned} \tag{6}$$

with $e = |e|$, and where the trace is taken in Nambu space with Nambu/lead (η/α) matrix Green's functions for the quantum dots defined as

$$G^{R,A}_{\alpha\eta,\alpha'\eta'}(t,t') = \mp i\theta(\pm t \mp t')\langle\{\phi_{\alpha\eta}(t), \phi^\dagger_{\alpha'\eta'}(t')\}\rangle, \tag{7}$$

$$\begin{aligned} G^<_{\alpha\eta,\alpha'\eta'}(t,t') &= i\langle\phi^\dagger_{\alpha'\eta'}(t')\phi_{\alpha\eta}(t)\rangle, \\ G^>_{\alpha\eta,\alpha\eta'}(t,t') &= -i\langle\phi_{\alpha\eta}(t)\phi^\dagger_{\alpha'\eta'}(t')\rangle, \end{aligned} \tag{8}$$

with self-energies, which are exact to second order in dot-lead tunneling,

$$\Sigma^{R,A,<}_\alpha(t) = \sum_k \mathcal{T}^*_\alpha g^{R,A,<}_{\alpha k}(t)\mathcal{T}_\alpha, \tag{9}$$

where $g_{\alpha k}$ denotes the Nambu Green's function in lead α. From this self-energy, the dot Green's functions can be found by solving the steady-state Dyson equations,

$$\begin{aligned} G^{R/A}(t,t') = G^{R/A(0)}(t,t_1) + \int dt_1 dt_2 G^{R/A(0)}(t,t_1) \\ \times \Sigma^{R/A}(t_1-t_2)G^{R/A}(t_2,t'), \end{aligned} \tag{10}$$

$$\begin{aligned} G^<(t,t') = \int dt_1 dt_2 G^R(t,t_1)\Sigma^<(t_1-t_2) \\ \times G^A(t_2,t'), \end{aligned} \tag{11}$$

with matrix products between Green's functions implied.

With a periodic drive, it is convenient to transform these two-time Green's functions into Floquet matrices [75]

$$O_{nm}(\omega) = \int_{-\infty}^{\infty} dt' \frac{1}{T}\int_0^T dt\; e^{i(\omega+n\Omega)t - i(\omega+m\Omega)t'} O(t,t'), \tag{12}$$

defined with $\omega \in]-\Omega/2, \Omega/2]$. This transformation presumes that the Green's functions are periodic in both time arguments, with the driving period $T = 2\pi/\Omega$, and thereby rests on the assumption that the system has reached a nonequilibrium steady state (NESS). In this way, the time-averaged current, $J = J_L = -J_R$, may be found from the zeroth Floquet components,

$$\begin{aligned} J_\alpha &= \frac{1}{T}\int_0^T dt\, I_\alpha(t) \\ &= 2(-e)\text{Tr}\Bigg\{\sigma_z\text{Re}\Bigg[\int_{-\Omega/2}^{\Omega/2} d\omega\,\big(G^R_{d,\alpha\alpha}(\omega)\Sigma^<_\alpha(\omega) \\ &\quad + G^<_{d,\alpha\alpha}(\omega)\Sigma^A_\alpha(\omega)\big)\Bigg]\Bigg\}. \end{aligned} \tag{13}$$

Here, the Green's functions and self-energies are matrices in Nambu, and Floquet space and the trace is performed over both. The components of the self-energy in dot, and Floquet space are given by

$$\Sigma^{R,A,<}_{\alpha,nm}(\omega) = \mathcal{T}^*_\alpha g^{R,A,<}_\alpha(\omega + n\Omega)\mathcal{T}_\alpha\delta_{nm}, \tag{14}$$

where the momentum-summed lead Nambu Green's functions are given explicitly as

$$g^{R,A}_\alpha(\omega) = \pi\nu_F\frac{-(\omega \pm i0_+)\sigma^0 + \Delta\sigma^x}{\sqrt{\Delta^2 - (\omega \pm i0_+)^2}}, \tag{15}$$

$$g^<_\alpha(\omega) = n_F(\omega)\big(g^A_\alpha(\omega) - g^R_\alpha(\omega)\big), \tag{16}$$

where n_F denotes the Fermi function. Henceforth, temperature is assumed to be zero.

Finally, using the Dyson equation (10), the retarded double-dot Green's function is found by inverting the following infinite-dimensional Floquet matrix of 4×4 matrices in Nambu-dot space:

$$\begin{aligned} \big(G^{R,A}_d(\omega)\big)^{-1}_{\alpha\alpha',nm} = \big\{ &-t_d\sigma^z\tau^x_{\alpha\alpha'} + \big[(\omega+n\Omega)\sigma^0 \\ &- \mathcal{T}^*_\alpha g^{R,A}_\alpha(\omega+n\Omega)\mathcal{T}_\alpha - \varepsilon_d\sigma^z\big]\tau^0_{\alpha\alpha'}\big\}\delta_{nm} \\ &- \frac{A}{2}(e^{-i\theta_\alpha/2}\delta_{n-m,1} + e^{i\theta_\alpha/2}\delta_{m-n,1})\sigma^z\tau^0_{\alpha\alpha'}. \end{aligned} \tag{17}$$

From the resulting retarded and advanced Green's functions, the lesser function is found from Eq. (11) by simple matrix multiplication.

IV. INFINITE-GAP LIMIT WITH WEAK INTERDOT TUNNEL COUPLING

It is instructive to first consider the analytically tractable limit of an infinite superconducting gap. This limit prohibits quasiparticle tunneling altogether and transport therefore takes place only via Cooper pairs. It captures much of the physics of the bound states, including a singlet to doublet ground state transition in the presence of interactions [45,51]. In the infinite-gap limit, the retarded QD self-energy becomes

$$\mathcal{T}_\alpha^* g_\alpha^{R,A}(\omega+n\Omega)\mathcal{T}_\alpha \approx -\Gamma e^{-i\sigma_z\varphi_\alpha}\sigma_x, \tag{18}$$

with $\Gamma=\pi\nu_F|t|^2$, corresponding to an effective Hamiltonian describing a proximitized quantum dot with an induced superconducting gap of Γ:

$$H_\infty(t)=\sum_{\alpha=L,R}\phi_\alpha^\dagger[\varepsilon_{d\alpha}(t)\sigma^z-\Gamma\sigma^x]\phi_\alpha + \phi_L^\dagger\mathcal{T}_d\phi_R+\phi_R^\dagger\mathcal{T}_d^*\phi_L, \tag{19}$$

with a matrix of tunneling amplitudes given by $\mathcal{T}_{d,\eta\eta'}=|t_d|\sigma^z_{\eta\eta'}\exp(i\sigma^z_{\eta\eta'}\varphi_{sc}/2)$, where $\varphi_{sc}=\varphi_L-\varphi_R$.

In order to illustrate the basic microwave-assisted Cooper pair transport mechanism within this infinite-gap model, we calculate here the weak-coupling tunneling charge current from right, to left dot, to second order in the interdot coupling t_d, given by the perturbative expression [76]

$$I(t)=2(-e)|t_d|^2\mathrm{Re}\Bigg[\int_0^t dt'\sigma^z_{\eta'\eta'}e^{i\left(\sigma^z_{\eta'\eta'}-\sigma^z_{\eta\eta}\right)\varphi_{sc}/2} \times\left(G^>_{L\eta,L\eta'}(t,t')G^<_{R\eta',R\eta}(t',t) - G^<_{L\eta,L\eta'}(t,t')G^>_{R\eta',R\eta}(t',t)\right)\Bigg]. \tag{20}$$

The driving enters this expression through the time-dependent correlation functions, $G^{<,>}_{\alpha\eta,\alpha\eta'}(t,t')$, describing the dynamics of the QD proximitized by lead $\alpha=L,R$.

The perturbative expression for the current requires the Green's functions for $t_d=0$, and in this case the Hamiltonian (19) describes two independent quantum dots. It is readily diagonalized by the time-dependent Bogoliubov transformation (suppressing the QD index, $\alpha=L,R$):

$$\chi_\nu=U_{\nu\eta}\phi_\eta,\quad \chi_\nu^\dagger=\phi_\eta^\dagger U^{-1}_{\eta\nu}, \tag{21}$$

with Nambu spinors

$$\chi=\begin{pmatrix}\gamma_\uparrow\\ \gamma_\downarrow^\dagger\end{pmatrix},\quad \phi=\begin{pmatrix}d_\uparrow\\ d_\downarrow^\dagger\end{pmatrix}, \tag{22}$$

and time-dependent unitary transformation matrix

$$U(t)=\begin{pmatrix}u(t) & -v(t)\\ v(t) & u(t)\end{pmatrix},\quad U^{-1}(t)=U^T(t), \tag{23}$$

with $E_d(t)=\sqrt{\varepsilon_d^2(t)+\Gamma^2}$ and real coherence factors given by

$$u(t)=\sqrt{[1+\varepsilon_d(t)/E_d(t)]/2},\qquad v(t)=\sqrt{[1-\varepsilon_d(t)/E_d(t)]/2}. \tag{24}$$

Notice that we omit the $\alpha=L,R$ subscript for clarity since it only enters in the two different phase shifts, θ_α, and can readily be reinstalled. This transformation diagonalizes the Hamiltonian for each of the two different proximitized levels,

$$H^0_\infty(t)=\phi^\dagger[\varepsilon_d(t)\sigma^z-\Gamma\sigma^x]\phi=\ \chi^\dagger E_d(t)\sigma^z\chi\,, \tag{25}$$

and endows the quasiparticles with dynamics governed by the equation of motion,

$$i\frac{d}{dt}\chi_\nu(t)=\left[E_d(t)\sigma^z_{\nu\nu'}+\frac{A\Omega\Gamma\sin(\Omega t+\theta)}{2E_d^2(t)}\sigma^y_{\nu\nu'}\right]\chi_{\nu'}(t), \tag{26}$$

where the last term has been obtained as

$$-iU_{\nu\eta}(t)\left(\frac{d}{dt}U^{-1}_{\eta\nu'}(t)\right)=\frac{A\Omega\Gamma\sin(\Omega t+\theta)}{2E_d^2(t)}\sigma^y_{\nu\nu'}. \tag{27}$$

The corresponding transformation of the correlation functions reads

$$G^<_{\eta\eta'}(t,t')=iU^{-1}_{\eta\nu}(t)U_{\nu'\eta'}(t')\langle\chi^\dagger_{\nu'}(t')\chi_\nu(t)\rangle,\qquad G^>_{\eta\eta'}(t,t')=-iU^{-1}_{\eta\nu}(t)U_{\nu'\eta'}(t')\langle\chi_\nu(t)\chi^\dagger_{\nu'}(t')\rangle. \tag{28}$$

The many-body eigenstates of the uncoupled and undriven QD are the empty QD, $|0\rangle$, the single-electron doublet, $|\sigma\rangle=d^\dagger_\sigma|0\rangle$, and the doubly occupied QD, $|2\rangle=d^\dagger_\uparrow d^\dagger_\downarrow|0\rangle$, with energies 0, ε_d, ε_d, and $2\varepsilon_d$, respectively. For the proximitized QD, the BCS-like ground state becomes $|\tilde{0}\rangle=u|0\rangle+v|2\rangle$, the excited doublet, $|\sigma\rangle$, remains unchanged, and the highest excited state becomes $|\tilde{2}\rangle=u|2\rangle-v|0\rangle$, with energies 0, E_d, E_d, and $2E_d$, respectively [cf. Fig. 2(a)].

When the system is driven with low amplitude, $A\ll E_d$, close to resonance, i.e., $\Omega\approx 2E_d$, transport can take place as indicated in Fig. 2(b) to second order in t_d. Since the mixing term (27) is already proportional to driving amplitude, A, we shall neglect the time dependence of $E_d(t)$ in its denominator and in coherence factors u and v, assuming that $A\ll\max(\epsilon_d,\Gamma)$. This allows us to include the mixing term (27) within a rotating-wave approximation (RWA), which leads to the following equation of motion:

$$i\frac{d}{dt}\chi_\nu(t)\approx\left[E_d\sigma^z_{\nu\nu'}+ge^{-i(\Omega t+\theta)\sigma^z_{\nu\nu}}\sigma^x_{\nu\nu'}\right]\chi_{\nu'}(t), \tag{29}$$

where $g=A\Omega\Gamma/(2E_d)^2$. This equation is readily solved by

$$\chi_\nu(t)=e^{-i\sigma^z_{\nu\nu}(\Omega t+\theta)/2}\tilde{U}^{-1}_{\nu\mu}\zeta_\mu(t), \tag{30}$$

with a secondary unitary transformation as

$$\tilde{U}^{-1}_{\nu\nu'}=\begin{pmatrix}\tilde{u} & \tilde{v}\\ -\tilde{v} & \tilde{u}\end{pmatrix}_{\nu\nu'}, \tag{31}$$

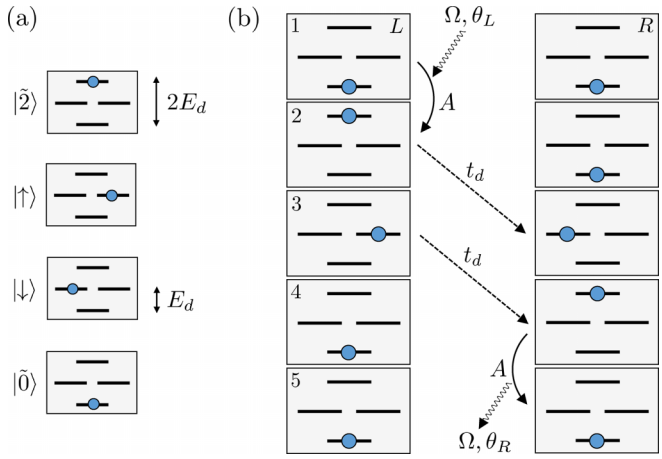

FIG. 2. (a) A schematic of the four many-body eigenstates of a single proximitized undriven QD. The ground state has zero energy, the excited doublet has energy E_d, and the two-quasiparticle state has energy $2E_d$. (b) Diagram illustrating the path of a Cooper pair through the driven DQD junction in progression from panels 1–5. Driving the microwave gates with $\Omega \sim 2E_d$ induces a near resonant transition from $|\tilde{0}\rangle$ to $|\tilde{2}\rangle$ in the left QD (1 and 2), followed by a two-step excitation transfer to the right QD via t_d (2–4), which finally decays via its own microwave gate (4 and 5).

defined in terms of

$$\tilde{u} = \sqrt{(1+\delta/\tilde{E})/2}, \quad \tilde{v} = \sqrt{(1-\delta/\tilde{E})/2}. \tag{32}$$

Here, $\delta = E_d - \Omega/2$ is the detuning, and the Rabi energy $\tilde{E} = \sqrt{\delta^2 + g^2}$ captures the slow time evolution of the corotating Nambu spinor

$$\zeta_\mu(t) = \zeta_\mu(0) e^{-i\tilde{E}t\sigma^z_{\mu\mu}}, \tag{33}$$

with initial condition $\zeta_\mu(0) = e^{i\sigma^z_{\nu\nu}\theta/2}\tilde{U}_{\mu\nu}\chi_\nu(0)$.

For concreteness, we assume both proximitized quantum dots to be in their ground state, $|\tilde{0}\rangle$, at time $t = 0$. Using the relations

$$\chi_\nu(0)|\tilde{0}\rangle = \delta_{\nu,2}|\downarrow\rangle, \quad \chi^\dagger_\nu(0)|\tilde{0}\rangle = \delta_{\nu,1}|\uparrow\rangle, \tag{34}$$

the time-evolved states are found as

$$\chi_\nu(t)|\tilde{0}\rangle = X_\nu(t)|\downarrow\rangle, \quad \chi^\dagger_\nu(t)|\tilde{0}\rangle = i\tau^y_{\nu\nu'}X_{\nu'}(t)|\uparrow\rangle, \tag{35}$$

with

$$X(t) = \begin{pmatrix} e^{-i\Omega t/2}e^{-i\theta}i(g/\tilde{E})\sin(\tilde{E}t) \\ e^{i\Omega t/2}\big(\cos(\tilde{E}t) + i(\delta/\tilde{E})\sin(\tilde{E}t)\big) \end{pmatrix}. \tag{36}$$

Reinstating the lead index α on θ and inserting this into Eq. (28), one finally arrives at the correlation functions

$$\begin{aligned} G^<_{\alpha\eta,\alpha\eta'}(t,t') &= i(b_\alpha(t), a_\alpha(t))_\eta (b^*_\alpha(t'), a^*_\alpha(t'))_{\eta'}, \\ G^>_{\alpha\eta,\alpha\eta'}(t,t') &= -i(a^*_\alpha(t), -b^*_\alpha(t))_\eta (a_\alpha(t'), -b_\alpha(t'))_{\eta'}, \end{aligned} \tag{37}$$

with generalized time-dependent coherence factors,

$$\begin{aligned} a_\alpha(t) &= e^{i\theta_\alpha/2}(-v, u)_\nu X_{\alpha\nu}(t), \\ b_\alpha(t) &= e^{i\theta_\alpha/2}(u, v)_\nu X_{\alpha\nu}(t), \end{aligned} \tag{38}$$

satisfying $|a_\alpha(t)|^2 + |b_\alpha(t)|^2 = 1$. The time-dependent current in Eq. (20) may now be expressed as

$$\begin{aligned} I(t) = 4(-e)|t_d|^2 \mathrm{Re}\Big[a^*_L(t) b^*_R(t) \int_0^t dt' (a_L(t') b_R(t') \\ + b_L(t') a_R(t') e^{-i\varphi_{sc}}) - (L \leftrightarrow R, \varphi_{sc} \leftrightarrow -\varphi_{sc}) \Big], \end{aligned} \tag{39}$$

involving time-local interdot pair amplitudes like

$$\begin{aligned} a_L(t) b_R(t) = i(u^2 e^{i\theta_d/2} - v^2 e^{-i\theta_d/2})(g/\tilde{E})\sin(\tilde{E}t) \\ \times [\cos(\tilde{E}t) + i(\delta/\tilde{E})\sin(\tilde{E}t)] \\ + uv\Big\{ e^{-i(\Omega t + \bar{\theta})}(g/\tilde{E})^2 \sin^2(\tilde{E}t) \\ + e^{i(\Omega t+\bar{\theta})}[\cos(\tilde{E}t) + i(\delta/\tilde{E})\sin(\tilde{E}t)]^2 \Big\}, \end{aligned} \tag{40}$$

with $\theta_d = \theta_L - \theta_R$ and $\bar{\theta} = (\theta_L + \theta_R)/2$.

This result relies on the weak-amplitude assumption of neglecting the time dependence of $E_d(t)$ in Eq. (26) and the subsequent RWA, which is expected to hold only close to resonance, i.e., for $\delta, g \ll \Omega$ [54]. In the undriven limit, $g \to 0$, the product in Eq. (40) reduces to

$$a_L(t) b_R(t) = uv e^{i(2E_d t + \bar{\theta})},$$

which leads to the time-dependent current

$$\begin{aligned} I(t) &= \frac{e|t_d|^2\Gamma^2}{\varepsilon_d^2 + \Gamma^2} \sin(\varphi_{sc}) \mathrm{Re}\Big[2ie^{-2iE_d t} \int_0^t dt' e^{2iE_d t'} \Big] \\ &= \frac{e|t_d|^2\Gamma^2}{\big(\varepsilon_d^2 + \Gamma^2\big)^{3/2}} \sin(\varphi_{sc})[1 - \cos(2E_d t)]. \end{aligned} \tag{41}$$

The time-dependent part, which derives from the $t = 0$ limit of the integral, vanishes under long-time averaging leaving only the equilibrium supercurrent

$$J = \lim_{t_I \to \infty} \frac{1}{t_I} \int_0^{t_I} dt\, I(t) = \frac{e|t_d|^2\Gamma^2}{\big(\varepsilon_d^2 + \Gamma^2\big)^{3/2}} \sin(\varphi_{sc}). \tag{42}$$

In the other limit, where $\delta = 0$, the system is driven exactly at resonance, and one finds that all terms in $I(t)$ become sinusoidal and the long-time average of the current vanishes altogether. Notice that this is regardless of φ_{sc}, meaning that to leading order in t_d the resonant drive washes out the equilibrium supercurrent carried by the undriven system.

In the general case of finite coupling, g, and finite detuning, δ, the last two terms in Eq. (40) will generally be suppressed by the fast oscillating phase factors, and we may therefore retain only the first slowly oscillating term, which carries no information about $\bar{\theta}$ and only depends on the phase difference, θ_d. These products reduce to

$$\begin{aligned} a_L(t) b_R(t) &\approx -f(\theta_d) h(t), \\ a_R(t) b_L(t) &\approx -f(-\theta_d) h(t), \end{aligned} \tag{43}$$

with

$$\begin{aligned} f(\theta_d) &= \frac{\varepsilon_d}{E_d}\cos(\theta_d/2) + i\sin(\theta_d/2), \\ h(t) &= \frac{\delta g}{\tilde{E}^2}\sin^2(\tilde{E}t) - i\frac{g}{2\tilde{E}}\sin(2\tilde{E}t). \end{aligned} \tag{44}$$

Finally, introducing $\kappa(\theta_d, \varphi_{sc}) = f(\theta_d)e^{i\varphi_{sc}/2} = \kappa' + i\kappa''$, the current takes the following form:

$$\begin{aligned} I(t) \approx & 8(-e)|t_d|^2 \mathrm{Re}\left[\kappa^*(\theta_d,\varphi_{sc})h^*(t)\int_0^t dt' h(t')\right]\kappa'(\theta_d,\varphi_{sc}) \\ & - (\theta_d \leftrightarrow -\theta_d, \varphi_{sc} \leftrightarrow -\varphi_{sc}) \\ = & -2e|t_d|^2 \frac{\delta g^2}{\tilde{E}^4}\kappa'(\theta_d,\varphi_{sc})\kappa''(\theta_d,\varphi_{sc}) \\ & [2\tilde{E}t\sin(2\tilde{E}t) - \sin^2(2\tilde{E}t) - 4\sin^4(\tilde{E}t)]. \end{aligned} \tag{45}$$

The long-time average becomes

$$\begin{aligned} & \lim_{t_I\to\infty}\frac{1}{t_I}\int_0^{t_I} dt(\sin^2(2\tilde{E}t) + 4\sin^4(\tilde{E}t) - 2\tilde{E}t\sin(2\tilde{E}t)) \\ & = 2 + \cos(2\tilde{E}t_I), \end{aligned} \tag{46}$$

which still depends on the integration time, t_I, but with a well-defined long-time average deriving from the first term, which leads to

$$\begin{aligned} J = & 4e|t_d|^2\frac{\delta g^2}{\tilde{E}^4}\kappa''(\theta_d,\varphi_{sc})\kappa'(\theta_d,\varphi_{sc}) \\ \approx & \frac{4e|t_d|^2A^2\Gamma^2}{E_d^2}\frac{(2E_d-\Omega)}{[(2E_d-\Omega)^2+(A\Gamma/E_d)^2]^2} \\ & \times\left[\left(\frac{\varepsilon_d^2}{E_d^2}\cos^2(\theta_d/2) - \sin^2(\theta_d/2)\right)\sin(\varphi_{sc})\right. \\ & \left.+\left(\frac{\varepsilon_d}{E_d}\sin(\theta_d)\right)\cos(\varphi_{sc})\right] \\ = & \frac{4e|t_d|^2A^2\Gamma^2}{E_d^2}\frac{(2E_d-\Omega)}{[(2E_d-\Omega)^2+(A\Gamma/E_d)^2]^2} \\ & \times\left(1-\frac{\Gamma^2}{E_d^2}\cos^2(\theta_d/2)\right)\sin(\varphi_{sc}+\varphi_0), \end{aligned} \tag{47}$$

with the phase shifted by

$$\begin{aligned} \varphi_0 = & \arctan\left(\frac{2\varepsilon_d E_d\tan(\theta_d/2)}{\varepsilon_d^2 - E_d^2\tan^2(\theta_d/2)}\right) \\ & + \pi\theta(E_d|\tan(\theta_d/2)| - \varepsilon_d). \end{aligned} \tag{48}$$

This expression is valid to leading order in t_d, close to resonance, $|\Omega - 2E_d| \ll \Omega$, and for weak drive amplitude $A\Gamma \ll \Omega^2$. The fast rotating terms which we have neglected in this expression are formally smaller by factors δ/Ω and g/Ω and provide for the following correction to the long-time average current (47):

$$\begin{aligned} \delta J = & \frac{4e|t_d|^2\delta}{16E_d^2(g^2+\delta^2)^2[4(g^2+\delta^2)-\Omega^2]} \\ & \times\Big(16g\Gamma(g^2+\delta^2)\cos(\bar{\theta})[E_d\cos(\varphi_{sc}/2)\sin(\theta_d/2) \\ & + \varepsilon_d\sin(\varphi_{sc}/2)\cos(\theta_d/2)] \\ & + \Gamma^2\sin(\varphi_{sc})[2g^2\delta(3\delta-4\Omega) \\ & - 9g^4 + \delta^3(15\delta-8\Omega)]\Big), \end{aligned} \tag{49}$$

which tends towards the undriven result, Eq. (42), in the limit of $g \to 0$ with $g \ll \delta \ll \Omega$.

The time-averaged current in Eq. (47) switches sign, when tuning the drive across resonance at $\Omega = 2E_d$ from red ($\delta > 0$), to blue ($\delta < 0$) detuning. This can be traced back to the fact that each of the driven quantum dots Rabi oscillates between states $|\tilde{0}\rangle$ and $|\tilde{2}\rangle$, with time-averaged probabilities of finding the QD in either state given by $P_{\tilde{0}/\tilde{2}} = (1 \pm \delta^2/\tilde{E}^2)/2$.

Since the time-dependent current in Eq. (39) has opposite sign when choosing the initial state to be $|\tilde{2}\rangle$, this implies that the total current averages to zero when the system is driven at resonance, $\delta = 0$. Likewise, the long-time average of the interdot pair amplitude (40) comprising the current in Eq. (41) reduces to

$$\begin{aligned} \langle a_L b_R\rangle = & \lim_{t_I\to\infty}\frac{1}{t_I}\int_0^{t_I} dt\, a_L(t)b_R(t) \\ = & -\frac{g\delta}{2\tilde{E}^2}f(\theta_d), \end{aligned} \tag{50}$$

which is linear in the detuning and vanishes at resonance. The average current attains its maximum for $\Omega = 2E_d \pm A\Gamma/(\sqrt{3}E_d)$ with

$$\begin{aligned} \langle I\rangle_{\max} \approx & \frac{3\sqrt{3}e|t_d|^2E_d}{4A\Gamma}\left(\frac{\varepsilon_d^2}{E_d^2}\cos^2(\theta_d/2) + \sin^2(\theta_d/2)\right) \\ & \times\sin(\varphi_{sc}+\varphi_0). \end{aligned} \tag{51}$$

One should keep in mind that the counter-rotating terms neglected within the RWA will lead to a Bloch-Siegert shift [54] of the resonance frequency of the order of $A^2/E_d \ll 1$, and for strong enough drive amplitudes the RWA breaks down altogether.

Tuning the levels away from the Fermi level, i.e., for $|\varepsilon_d| \gg \Gamma$, we have $E_d \approx |\varepsilon_d|$ and the current becomes

$$J \approx \frac{4e|t_d|^2A^2\Gamma^2}{\varepsilon_d^2}\frac{(2|\varepsilon_d|-\Omega)\sin[\varphi_{sc}+\varphi_0(\theta_d)]}{[(2|\varepsilon_d|-\Omega)^2+(A\Gamma/\varepsilon_d)^2]^2}, \tag{52}$$

which is a Floquet φ_0 junction with

$$\varphi_0(\theta_d) = \mathrm{sgn}(\varepsilon_d)\theta_d + \pi\,\theta[-\cos(\theta_d)], \tag{53}$$

exhibiting a sharp sign change in current when $\cos(\theta_d)$ passes through zero.

In the opposite limit, where the two levels are close to the Fermi levels of the two superconducting leads, i.e., $|\varepsilon_d| \ll \Gamma$, we have $E_d \approx \Gamma$ and arrive at

$$J \approx 4e|t_d|^2A^2\frac{(2\Gamma-\Omega)\sin^2(\theta_d/2)}{[(2\Gamma-\Omega)^2+A^2]^2}\sin(\varphi_{sc}), \tag{54}$$

which corresponds to a normal Josephson 0 junction below resonance ($\Omega < 2\Gamma$), and a π junction above resonance ($\Omega > 2\Gamma$). In this limit, the phase shift of the two drives, θ_d, serves only to modulate the amplitude, attaining maximum critical time-averaged current when the drives are shifted by $\theta_d = \pi$, and blocking it altogether for $\theta_d = 0$.

This average current was calculated under the assumption of an even number of electrons occupying each of the two levels, with the specific initial condition that the system is in its lowest energy state at time zero. In a real system, however, quasiparticle poisoning and relaxation will cause occasional switching of the parity of each of the two levels, limiting the accessible integration time, t_I. With typical parity flip

times of the order of 20–200 μs [65,77–79], a resonant drive frequency, $\Omega \sim 2E_d$, of the order of 10 GHz, say, will take the system through some 10^6 drive cycles before the parity is flipped. The long-time average in Eq. (46) makes the current in Eq. (45) resemble the undriven result in Eq. (41), but with frequency down-converted from E_d to the much slower Rabi frequency $\tilde{E}$ and with amplitude given by Eq. (47). Within the validity of the RWA, $\tilde{E}/\Omega \sim 10^{-3}$, say, this down-converted current would still oscillate through some 10^3 Rabi periods between subsequent parity flips, leaving sufficient integration time to define a long-time average. The full problem incorporating the stochastic parity switching dynamics poses an interesting problem in itself, which we shall not pursue further in this work. Instead, we shall analyze the steady-state Dyson equation (11), in which the parity is relaxed in the infinite gap limit by a weak coupling to a normal metallic reservoir. For a finite gap, the Floquet sidebands of the continuum provide the same effect and the normal metallic reservoir is no longer needed.

Notice that the full lesser component of the Dyson equation has a second contribution [73], $(1 + G^R\Sigma^R)G_0^<(1 + \Sigma^A G^A)$, referring to the initial lesser function, and that this term has been omitted altogether in Eq. (11). This omission rests on the tacit assumption that $\Sigma^<$ contains relaxation mechanisms, which will wash out the initial conditions, i.e., that $\Sigma^< \gg G_0^{R,-1}G_0^<G_0^{A,-1} = (G_0^{R,-1} - G_0^{A,-1})f_0$, where f_0 denotes an initial distribution function. In the present tunneling problem, $\Sigma^<$ refers to quasiparticle tunneling to and from the superconducting leads and to the weak tunneling of electrons directly between the dots and a normal metal reservoir. The former contribution vanishes altogether in the infinite-gap limit, and the steady-state Dyson equation (11) as well as the Floquet-Keldysh transformation (12) are therefore justified in the infinite gap limit by the normal metal tunneling rate, Γ_m, which is large enough to dominate the finite $\eta = (G_0^{R,-1} - G_0^{A,-1})/(2i)$ used in our numerical implementation of the bare Green's functions of the leads, yet small enough not to affect the result.

V. NUMERICAL RESULTS

In this section we present the numerical results obtained with the Floquet-Keldysh Green's functions introduced in Sec. III. We shall focus entirely on the time-averaged quantities, which may be found as the zeroth Floquet components, and we shall narrow down the rather large parameter space to illustrate some of the most interesting time-averaged current-phase relations realized by this driven junction.

In practice, the inversion of the Nambu-Floquet matrix (17) is carried out by truncating to the $n_{\max}$ lowest Floquet modes, i.e., working with square matrices of dimension $4(1 + 2n_{\max})$. For all numerical results presented below, we ensure that $n_{\max}$ is large enough that increasing it further does not affect the results. Furthermore, we use a finite broadening in the lead Green's functions, replacing 0_+ by $\eta = 10^{-4}$ in Eq. (15), which, like all energy and frequency ($\hbar \equiv 1$) parameters used below (except for the infinite-gap limit), is specified in units of Δ. In order to facilitate the numerical integration over the sharp subgap states in the infinite-gap limit, both levels are weakly coupled to a normal metallic lead with chemical potential aligned with the two superconducting leads, $\mu_m = 0$. This gives rise to a finite imaginary part, Γ_m, of the d-electron self-energies (14), which is chosen to be smaller than any other scale in the problem, yet resolved by the discretized numerical integrations. In practice, this corresponds to a finite parity relaxation time, which is longer than any other timescale in the problem. As discussed in the previous section, this also constitutes the formal justification of the steady-state Dyson equation (11). For a finite gap, the continuum of the superconducting leads provides the necessary broadening for the numerical calculations, and the normal metallic lead is not needed.

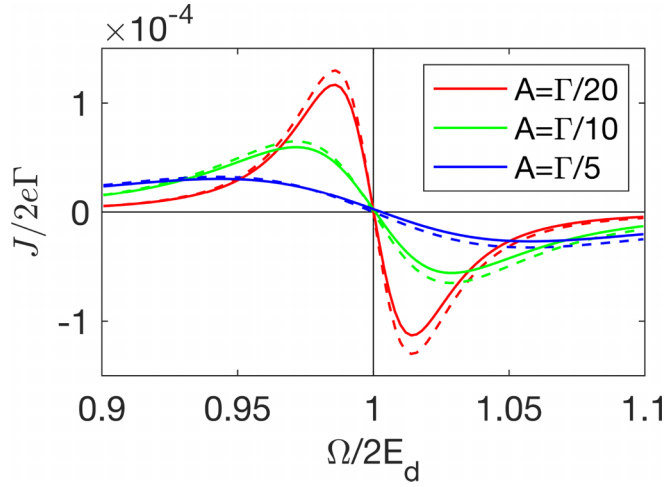

FIG. 3. Dashed lines: Plots of the weak-coupling anomalous Josephson ($\varphi_{sc} = 0$) current in Eq. (47) in the infinite-gap limit as a function of the driving frequency, showing the maxima on each side of the node right at resonance, $\Omega = 2E_d$. Parameters are chosen such that $t_d = \Gamma/100$, $\varepsilon_d = \Gamma/10$, and $\theta_d = \pi/2$, together with three different driving amplitudes (see inset). Full lines: Numerical calculation of the current using Eq. (6) with the same parameters as above and with $\Delta = 10^4$, $\eta = 10^{-4}$, and an additional broadening of the QD states corresponding to a normal metal tunneling rate $\Gamma_m = \Gamma/500$.

A. Infinite- and large-gap results

In order to connect to the results of the previous section, we first consider the large-gap limit, $\Delta \gg \Gamma$, in which all current is carried by Cooper pairs, at weak tunnel coupling and close to resonance. The resulting time-averaged current [cf. Eq. (6)] is shown in Fig. 3 as a function of the driving frequency in a narrow range around resonance. It is seen to match the perturbative results very well. Figure 4 shows the time-averaged current as a function of the two phase differences, φ_{sc} and θ_d, for a fixed driving frequency slightly below resonance. We show this together with two cuts illustrating a good match to Eq. (47).

Increasing the amplitude of the drive and fixing the driving phase shift at $\theta_d = \pi/2$, gives rise to highly nontrivial CPRs, of which a few examples are shown in Fig. 5. For a small driving amplitude ($A = 0.1\Gamma$ shown) the CPR is modified by narrow dips of the current, occurring at values of φ_{sc} for which an integer multiple of the driving frequency, Ω, becomes

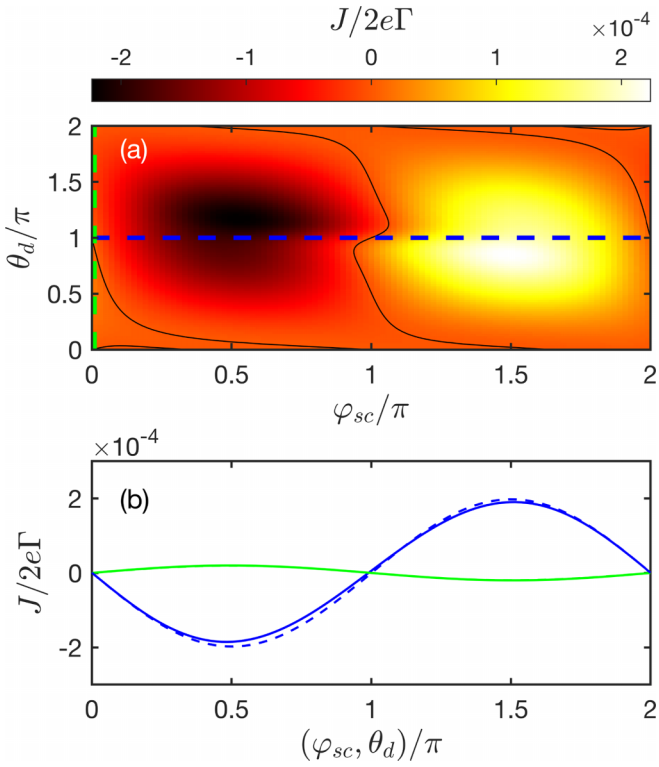

FIG. 4. (a) Density plot of the weak-coupling current vs superconductor phase difference and phase shift of the two drives obtained by numerical evaluation of Eq. (6). The current vanishes at the black solid lines. (b) Solid lines correspond to cuts along the dashed blue ($\theta_d = \pi$), and green ($\varphi_{sc} = 0$) lines indicated in the upper panel, together with the corresponding analytical infinite-gap weak-coupling current from Eq. (47) limit (dashed). In both panels, parameters are $t_d = \Gamma/100$, $A = \varepsilon_d = \Gamma/10$, and $\Omega = 2\Gamma$. In the numerical evaluation the infinite gap was replaced by $\Delta = 10^4$, while $\eta = 10^{-4}$ and $\Gamma_m = \Gamma/500$.

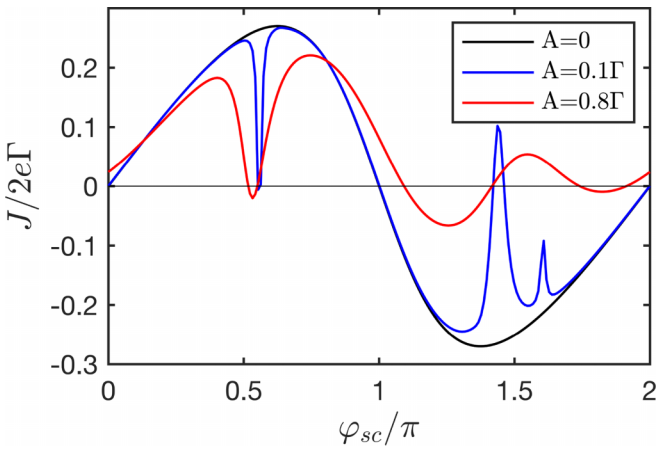

FIG. 5. Current-phase relation in the infinite-gap limit ($\Delta = 10^4\Gamma$) with and without drives of amplitude A, frequency $\Omega = 2.2\Gamma$, and phase shift $\theta_d = \pi/2$. Both levels have energy $\varepsilon_d = 0.8\Gamma$ with a weak normal metal tunneling rate $\Gamma_m = \Gamma/500$, and are tunnel coupled by $t_d = 2\Gamma$.

resonant with a subgap transition energy. This is similar to what is predicted for superconducting junctions with only a single drive [56,57], the main difference being that in the present case (like in Ref. [61]) the CPRs are not symmetric around $\varphi_{sc} = \pi$ and the resonant dips are not current nodes. For higher driving amplitudes ($A = 0.8\Gamma$ shown) the current is reduced, as for the junctions with only a single drive, but now the CPR is severely modified with no special significance of either $\varphi_{sc} = 0$ or $\varphi_{sc} = \pi$, both exhibiting finite supercurrent.

For comparison, in the Appendix we calculate the current using the same parameters as for the blue curve ($A = 0.1\Gamma$) in Fig. 5, but now using Floquet states to determine the time evolution starting from the nondriven even-parity ground state. This is done in the infinite-gap limit and with no coupling to a normal metal ($\Gamma_m = 0$), and the long-time average of the resulting current shows excellent correspondence with the steady-state current in Fig. 5 (cf. Fig. 10). Furthermore, intradot Coulomb interactions are straightforwardly included in this approach and are shown in Fig. 10 to remove the sharp dips in the current when the interaction strength becomes of the order of the driving frequency Ω. The systematic behavior relies on many parameters, but the main effect of the interactions is to change the resonance condition for the drive. In a real system with parity relaxation, increasing the interaction strength will of course stabilize an odd-parity ground state for the undriven system serving as a π junction [16,45].

B. Finite-gap results

Turning to the case of a finite BCS gap, i.e., the more realistic case where Δ is no longer much larger than all other energy scales, we first fix the superconductor phase difference to zero ($\varphi_{sc} = 0$) and plot the time-averaged current as a function of the drive frequency in the upper panel (a) of Fig. 6. The lower panel (b) shows the corresponding time-averaged density of states on the proximitized double quantum dot, exhibiting pronounced peaks at two slightly different ABS energies, split by the interdot tunnel coupling t_d, together with their weaker first, and even weaker second Floquet sidebands. From this plot, one may now understand the various features in the current.

Coming from large Ω, the small bump in the current near the vertical grid line labeled c corresponds to a resonance between the first sideband of the two ABS and the BCS quasiparticle continuum near $\Omega = \Delta + E_{ABS} \simeq 1.5\Delta$. At lower frequencies the current attains its largest magnitude slightly off resonance, and a node right at resonance, $\Omega \simeq 2E_{\mathrm{ABS}} \simeq 1.2\Delta$, near the vertical grid line labeled b. Here a positive ABS energy matches the first sideband of a negative ABS energy and vice versa, as illustrated in Fig. 2 for weak t_d. For lower frequencies near the vertical grid line labeled a, the current exhibits another bump, corresponding to crossings of ABS sidebands with each other or with the continuum. Apart from this additional structure arising from the finite gap or from a substantial driving amplitude, the overall frequency dependence of the current clearly resembles the resonant structure found in the infinite-gap limit in Fig. 3. For the rest of the paper, we fix the drive frequency to be slightly off the main resonance at $\Omega \simeq 2E_{\mathrm{ABS}}$ where this anomalous supercurrent attains it maximum.

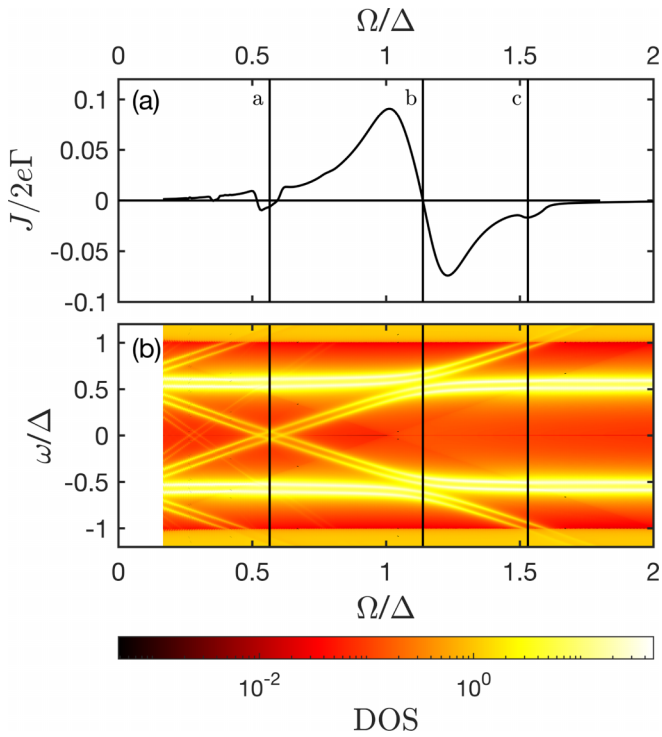

FIG. 6. (a) Time-averaged current at zero superconductor phase difference ($\varphi_{sc} = 0$) as a function of drive frequency. (b) Corresponding time-averaged density of states on the DQD. Both panels are evaluated with $\Delta = 3\Gamma/2$, $t_d = \Gamma$, $A = 0.4\Gamma$, $\varepsilon_d = 0.1\Gamma$, $\varphi_{sc} = 0$, $\theta_d = \pi/2$, and $n_{\max} = 7$.

To further investigate the effect of the continuum in the anomalous current we show in Fig. 7 how the current varies with Δ and Ω. Coming from high Δ, the resonant min-zero-max structure observed near $\Omega = 2E_{\rm ABS}$ in Figs. 3 and 6(a) persists down to a ratio of approximately $\Delta/\Gamma \simeq 2$–3, with only a slight shift in the resonance frequency. Notice also the

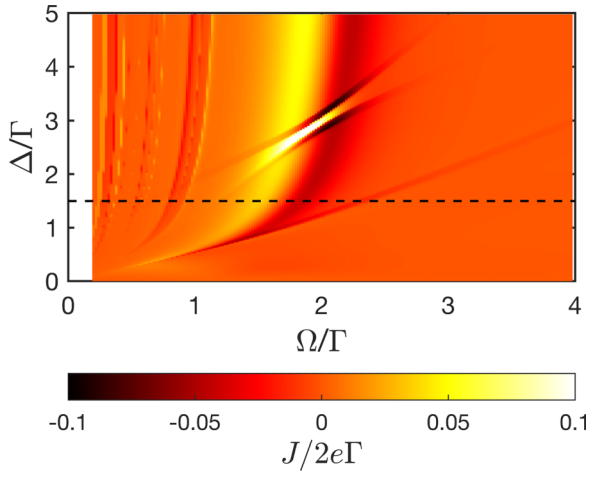

FIG. 7. Time-averaged current at zero superconductor phase difference ($\varphi_{sc} = 0$) as a function of drive frequency and BCS gap magnitude. Parameters are chosen as in Fig. 6: $t_d = \Gamma$, $A = 0.4\Gamma$, $\varepsilon_d = 0.1\Gamma$, $\varphi_{sc} = 0$, $\theta_d = \pi/2$, and $n_{\max} = 7$. The black dashed line at $\Delta = 3\Gamma$ is the cut shown in Fig. 6.

faint vertical features showing up at lower frequencies, which we ascribe to higher sideband resonances at $\Omega = 2E_{\rm ABS}/n$ with $n = 2, 3, \ldots$. For lower Δ, deviations from the infinite-gap limit become more pronounced. The current becomes very small and frequency independent, consistent with a weak adiabatic pumping of normal current, similar to the case with normal leads [80]. The line separating the two regions corresponds to the condition for resonance between the continuum and the first Floquet sideband to the negative energy ABS, i.e., $\Omega = \Delta + E_{\rm ABS}$, where the energy of the ABS itself also depends on the superconducting gap [44,50,56]. A second line with twice the slope is also observed. It corresponds to a resonance between the second Floquet sideband of the negative energy ABS and the quasiparticle continuum, beyond which the resonances carrying supercurrent are not modified. Interestingly, this second sideband is observed to anticross with the first sideband of the positive energy ABS, which gives rise to a large enhancement of the resonant current peak at frequency just below $\Omega = 2E_{\rm ABS}$. Since this anticrossing involves sidebands crossing with the continuum, this enhancement of the current is most likely due to a dissipative quasiparticle current. On the other hand, the nearly vertical features in this figure, including the most pronounced min-zero-max resonance, correspond to a current of Cooper pairs, which are being pumped across the junction by phase-shifted resonances between subgap states and their Floquet sidebands as indicated in Fig. 2.

C. Modified and rectifying current-phase relations

The time-averaged current can be tuned in a number of ways. In the previous sections, we have focused on the resonant aspect by tuning the external driving frequency, Ω, and the BCS gap, Δ. In this section, we keep these parameters fixed and study instead how the CPR of this driven DQD Josephson junction is modified by the level position, ε_d, and the driving phase shift, θ_d, respectively. As established in the Appendix for single-state time evolution in the infinite-gap limit, the symmetries of the Floquet Hamiltonian guarantee the following symmetries of the time-averaged current:

$$J(\varphi_{sc}, \theta_d, \varepsilon_d) = -J(-\varphi_{sc}, \theta_d, -\varepsilon_d), \tag{55}$$

$$= -J(-\varphi_{sc}, -\theta_d, \varepsilon_d). \tag{56}$$

As we shall see below, these symmetries are also respected when the current is calculated from steady-state Green's functions and with a finite BCS gap.

In Fig. 8(a), we show the time-averaged current as a function of superconducting phase difference, φ_{sc}, and level position, ε_d, with a driving phase shift of $\theta_d = \pi/2$. The current is calculated using the numerical steady-state Green's function approach and is observed to respect the symmetry relation expressed by Eq. (55). Three different cuts are shown in the lower panel (b). For $\varepsilon_d = 0$, the vertical black dashed cut illustrates the usual antisymmetry around $\varphi_{sc} = \pi$, and zero anomalous current at $\varphi_{sc} = 0$. This symmetry breaks down for $\varepsilon_d \neq 0$ and, as indicated by the vertical green dashed cut, may even lead to a unidirectional supercurrent, corresponding to *complete rectification*. The horizontal blue dashed cut, on the other hand, illustrates the antisymmetry of the current under

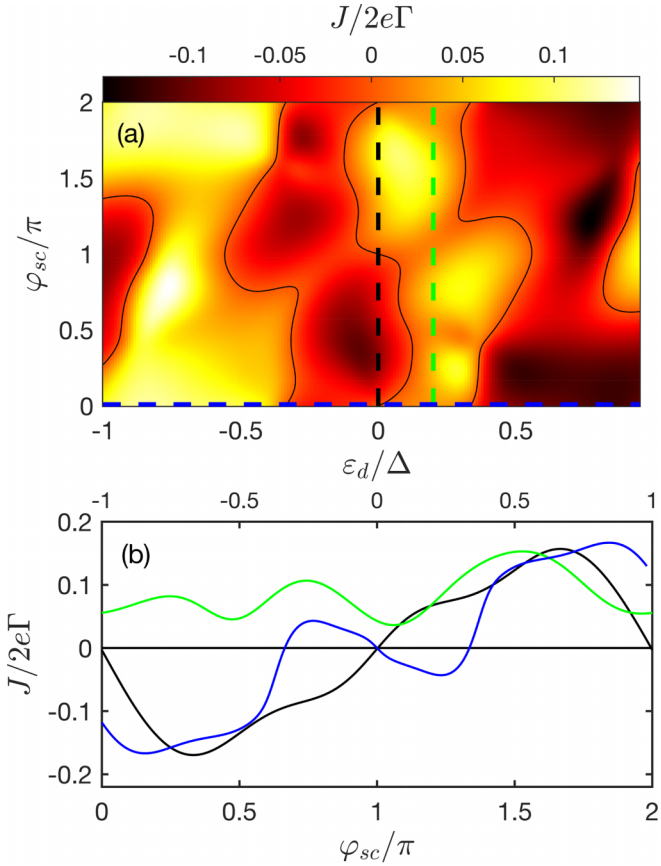

FIG. 8. (a) Density plot of the time-averaged current vs ε_d and φ_{sc}. The current vanishes at the black solid lines. (b) Cuts in panel (a) for, respectively, $\varphi_{sc} = 0$ (blue), $\varepsilon_d = 0$ (black), and $\varepsilon_d = 0.2\Delta$. The green cut at $\varepsilon_d = 0.2\Delta$ shows a completely rectified current, which remains positive for all values of φ_{sc}. In both panels, parameters are $2\Gamma = t_d = 0.7\Delta$, $A = 0.8\Delta$, $\Omega = 0.9\Delta$, $\theta_d = \pi/2$, and $n_{\max} = 7$.

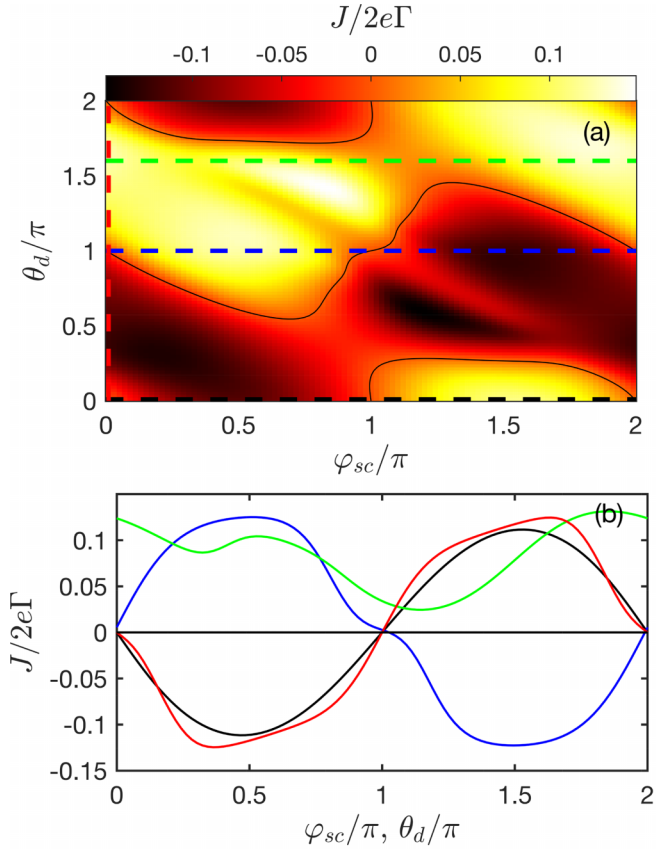

FIG. 9. (a) Density plot of the time-averaged current vs θ_d and φ_{sc}. The current vanishes at the black solid lines. (b) Cuts in panel (a) for, respectively, $\theta_d = \pi$ (blue), $\theta_d = 0$ (black), and $\varphi_{sc} = 0$ (red). The blue (black) cut constitutes a slightly anharmonic 0 (π) junction. The cut at $\theta_d = 1.6\pi$ (green line) shows a completely rectified current, which remains positive for all values of φ_{sc}. In both panels, parameters are $2\Gamma = t_d = 0.7\Delta$, $A = 0.8\Delta$, $\varepsilon_d = 0.8\Delta$, $\Omega = 0.9\Delta$, and $n_{\max} = 11$.

inversion of ε_d for $\varphi_{sc} = 0$. In Fig. 9(a), we show instead the time-averaged current as a function of superconducting phase difference, φ_{sc}, and level position, ε_d, with a driving phase shift of $\varepsilon_d = 0.8\Delta$. This plot is observed to respect the symmetry relation expressed by Eq. (56). Again, three different cuts are shown in the lower panel (b). The vertical red dashed cut shows the anomalous relation between time-averaged current and the driving phase shift, θ_d, with the superconductor phase difference fixed at $\varphi_{sc} = 0$. Akin to an ordinary π junction, the anomalous current attains its maximum near, although not right at, $\theta_d = \pi/2$. The three horizontal (black, blue, and green) dashed cuts illustrate the strongly modified CPRs for fixed θ_d. Switching from $\theta_d = 0$ to $\theta_d = \pi$, the driven Josephson junction is seen to switch the current-phase relation from a π to a 0 junction, as seen in the black and the blue curves, respectively, up to a slight anharmonicity in both. Once again, the green cut realizes a rectified time-averaged current. Since the BCS gap is finite, there is no guarantee that this completely rectified pump current is exclusively a current of Cooper pairs. Nevertheless, as we show in Fig. 12 in the Appendix a nearly completely rectified current can also be obtained in the infinite-gap limit where all current must be carried by Cooper pairs, indicating that there is no fundamental obstacle to attaining a unidirectional time-averaged supercurrent for all φ_{sc}.

VI. CONCLUSIONS

The microwave-enabled DQD Josephson junction studied here offers a highly tunable superconducting circuit element, in which the traversing supercurrent is controlled by two phase-shifted microwave tones applied to the individual gate voltages of each quantum dot. This driven device comprises an effective Josephson junction with a highly nontrivial CPR which can be tuned electronically. More specifically, the phase-shifted microwave drives induce an alternating tunneling current between the two superconducting leads, whose long-time average exhibits an anomalous and often highly anharmonic relation to the superconductor phase difference.

The supercurrent response to the driving relies on nonadiabatic resonant photon-assisted tunneling. This was established in the infinite-gap limit by means of perturbation theory and by time evolution of the nondriven ground state using Floquet theory (cf. Appendix). For a finite BCS gap, the steady-state

time-averaged current was calculated numerically by means of Floquet-Keldysh Green's functions. Whereas the general finite-gap current may include some fraction of normal current carried by BCS quasiparticles, the main resonant pump current arising when the drive frequency is slightly off resonance with the energy difference between the two subgap ABS was argued to be carried mainly by Cooper pairs.

For clarity, we have restricted our analysis to a symmetrically coupled device, where only the microwave phase shift breaks the L/R-inversion symmetry. None of the salient features demonstrated in this case rely critically on this symmetry, as can readily be assessed in the infinite-gap limit using the Floquet theory employed in the Appendix . Likewise, local Coulomb interactions, reflecting the finite charging energies of the quantum dots, are readily included within the infinite-gap Floquet theory and was shown in the Appendix to alter the resonance conditions and thereby affect the time-averaged current. Nevertheless, the anomalous Josephson effect (and the rectification) persisted, and was found to exhibit a 0-π transition in θ_d, as the interaction strength increased past a critical value. Furthermore, the symmetry relations, Eqs. (55) and (56), were generalized to the interacting case, and used to infer that the anomalous current vanishes more generally at the particle-hole symmetric point, $\varepsilon_d = -U/2$. Naturally, not all conclusions drawn from the infinite-gap limit need hold for the more realistic case where $U \gg \Delta$, which leads to the formation of Yu-Shiba-Rusinov states [47,51] and makes the corresponding analysis more complicated.

In light of the recent interest in Josephson diodes [81–84], we emphasize the fact that this driven Josephson junction offers complete rectification of the time-averaged supercurrent.

Note added. Recently, we became aware of a paper by Soori [85] pointing out a Josephson diode effect present in a nonadiabatically driven two-site SNS junction explored also in Ref. [70]. With this work we have demonstrated that complete rectification persists throughout a finite range of parameters. The more detailed requirements for rectification in driven junctions are relegated to future work.

ACKNOWLEDGMENTS

The Center for Quantum Devices (Project No. DNRF101) and the Center for Nanostructured Graphene (Project No. DNRF103) are funded by the Danish National Research Foundation. C.O.T. acknowledges funding from the Swedish Research Council under Grant No. 2017-05162. We acknowledge fruitful discussions with G. Steffensen, K. Flensberg, and M. Geier.

APPENDIX: FLOQUET ANALYSIS OF THE INTERACTING INFINITE-GAP LIMIT

The infinite-gap limit offers relatively easy access to the symmetries of the problem, which are also revealed by the steady-state numerical calculations presented in the main text. In this Appendix, we employ Floquet theory to provide a brief supplementary analysis of this more tractable limit, in which local Coulomb interactions on the quantum dots can readily be included. Furthermore, since no quasiparticle excitations are involved in the infinite-gap limit, all currents calculated below are carried exclusively by Cooper pairs. We choose to consider only the even-parity sector, but a similar analysis is straightforwardly made for the odd-parity sector.

In the even-parity sector, the Hilbert space is spanned by the basis $\{|00\rangle, |20\rangle, |02\rangle, |22\rangle, |\uparrow\downarrow\rangle, |\downarrow\uparrow\rangle\}$, where the left (right) index indicates the many-body states of the left (right) dot. In this basis the first quantized Hamiltonian reads

$$\hat{H}_{e,\infty} = \begin{pmatrix} 0 & -\Gamma & -\Gamma & 0 & 0 & 0 \\ -\Gamma & 2\varepsilon_d + U & 0 & -\Gamma & z & -z \\ -\Gamma & 0 & 2\varepsilon_d + U & -\Gamma & z^* & -z^* \\ 0 & -\Gamma & -\Gamma & 4\varepsilon_d + 2U & 0 & 0 \\ 0 & z^* & z & 0 & 2\varepsilon_d & 0 \\ 0 & -z* & -z & 0 & 0 & 2\varepsilon_d \end{pmatrix}, \tag{A1}$$

with tunneling matrix elements $z = t_d e^{i\varphi_{sc}/2}$, and with the local intradot Coulomb interaction, U, now included. From this, one may construct the even-parity Floquet Hamiltonian, H_e^F, corresponding to the harmonic driving term, $A\cos(\Omega t)$, from the matrix elements [86–88]

$$\hat{H}^F_{e,mn} = (\hat{H}_{e,\infty} - n\Omega\hat{I})\delta_{mn} + \hat{V}\delta_{n-m,1} + \hat{V}^\dagger\delta_{m-n,1}, \tag{A2}$$

where $\hat{I}$ denotes the 6×6 unit matrix, and $\hat{V}$ is defined as the 6×6 matrix with diagonal elements

$$A\left\{0, e^{i\theta_L}, e^{i\theta_R}, e^{i\theta_L} + e^{i\theta_R}, \frac{e^{i\theta_L} + e^{i\theta_R}}{2}, \frac{e^{i\theta_L} + e^{i\theta_R}}{2}\right\}, \tag{A3}$$

and zeros elsewhere. Truncating this infinite-dimensional matrix and solving the $6(2n_{\max}+1)$-dimensional eigenvalue problem

$$\sum_{n=-n_{\max}}^{n_{\max}} \hat{H}^F_{e,mn}|u^n_\nu\rangle = \epsilon_\nu|u^m_\nu\rangle, \tag{A4}$$

the time-dependent Schrödinger equation is solved by the six Floquet states,

$$|\psi_\nu(t)\rangle = e^{-i\epsilon_\nu t}\sum_{n=-n_{\max}}^{n_{\max}} e^{-in\Omega t}|u^n_\nu\rangle, \tag{A5}$$

corresponding to the six quasienergies in the first Floquet Brillouin zone, $-\Omega/2 < \epsilon_\nu < \Omega/2$, for $\nu = 1, 2, \ldots, 6$. Expressing these six eigenstates in the original six-dimensional even-parity basis, $|u^n_\nu\rangle = \sum_i u^n_\nu(i)|i\rangle$, a given initial state may

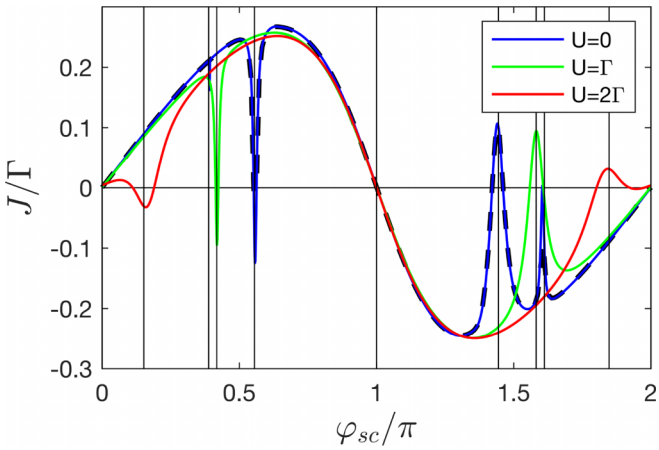

FIG. 10. Interaction dependence of the current-phase relations for parameters as in Fig. 5 ($\Omega = 2.2\Gamma$, $\theta_d = \pi/2$, $\varepsilon_d = 0.8\Gamma$, $t_d = 2\Gamma$), with $A = 0.1\Gamma$. Full lines correspond to the result obtained using the methods in this Appendix. Blue (green, red) lines correspond to $U = 0$ ($U = \Gamma$, $U = 2\Gamma$). Dashed black line is the same result as Fig. 5, also for $A = 0.1\Gamma$.

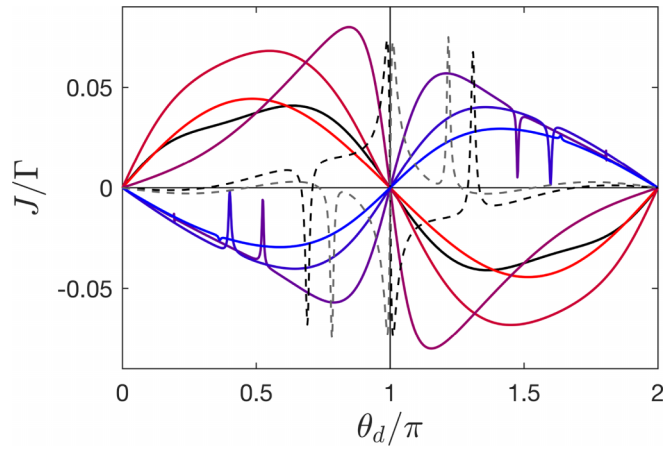

FIG. 11. Anomalous Josephson current at $\varphi_{sc} = 0$ versus driving phase difference, θ_d, for interaction strengths ranging from $U = 0$ (red) to $U = 5\Gamma$ (blue) in steps of Γ. A marked sign change in current takes place between $U = 2.3\Gamma$ (thin black dashed) and $U = 2.35\Gamma$ (thin gray dashed). Other parameters are as for the red curve in Fig. 5 ($\Omega = 2.2\Gamma$, $\theta_d = \pi/2$, $\varepsilon_d = 0.8\Gamma$, $t_d = 2\Gamma$, $A = 0.7\Gamma$, and $n_{\max} = 9$).

now be expressed as

$$|\Psi(0)\rangle = \sum_{\nu,i=1}^{6} c_\nu \sum_{n=-n_{\max}}^{n_{\max}} u_\nu^n(i)|i\rangle, \tag{A6}$$

from where the coefficients c_ν are found by inverting the square $(n\nu)$ matrices $u_\nu^n(i)$. Finally, the solution for the full time evolution of the state can be expressed as

$$|\Psi(t)\rangle = \sum_{\nu,i=1}^{6} c_\nu e^{-i\epsilon_\nu t} \sum_{n=-n_{\max}}^{n_{\max}} e^{-in\Omega t} u_\nu^n(i)|i\rangle. \tag{A7}$$

1. Time-averaged current

From this time-evolved state, the time-dependent expectation value of the charge current operator, $\hat{I} = (2e)\partial_{\varphi_{sc}}\hat{H}_{e,\infty}$, is determined as

$$\begin{aligned} I(t) &= \langle\Psi(t)|\hat{I}|\Psi(t)\rangle \\ &= 2e \sum_{\mu\nu,ij,mn} c_\mu^* c_\nu \left[u_\mu^m(j)\right]^* u_\nu^n(i) \\ &\quad \times e^{i(\epsilon_\mu - \epsilon_\nu + (m-n)\Omega)t} \langle j|\hat{I}|i\rangle, \end{aligned} \tag{A8}$$

which leads to the long-time average

$$\begin{aligned} J &= \lim_{t_I\to\infty} \frac{1}{t_I} \int_0^{t_I} dt\, I(t) \\ &= 2e \sum_{\nu,n,ij} |c_\nu|^2 \left[u_\nu^n(j)\right]^* u_\nu^n(i) \langle j|\hat{I}|i\rangle. \end{aligned} \tag{A9}$$

Using the same parameters as in Fig. 5 and choosing the ground state of the undriven system as the initial state, one may now calculate the matrices, $u_\nu^n(i)$, together with the corresponding coefficients, c_ν, and evaluate the time-averaged current using formula (A9). The result is shown in Fig. 10, with full blue (green, red) lines corresponding to $U = 0$ ($U = \Gamma, U = 2\Gamma$). For comparison, the Green's function result shown in Fig. 5 for $A = 0.1\Gamma$ is included here as the black dashed line. The two methods are in excellent agreement, and capture the same resonances, shown here to lie on top of the grid lines placed at the values of φ_{sc} at which an integer multiple of Ω matches a bound state transition energy. As U is increased, the effects of driving are diminished and at $U = 3\Gamma$ they are completely gone.

The red curve in Fig. 5, corresponding to $A = 0.7\Gamma$, displays a finite anomalous Josephson current at $\varphi_{sc} = 0$. In Fig. 11, we use the same parameters to show that this anomalous Josephson current depends strongly on the phase difference of the two drives, θ_d, as found also with a finite BCS gap in the red curve of the right panel of Fig. 9. Here, however, one observes also a sign change of the anomalous Josephson current, corresponding to a transition from a 0-to π-junction behavior in θ_d, when increasing the interaction strength. For the chosen parameters, this takes place at a critical interaction strength, $U_c \sim \Omega$, but the more detailed parametric dependence of U_c is beyond the scope of this paper.

Finally, with Fig. 12, we demonstrate that nearly complete rectification of the time-averaged current is possible also in the infinite-gap limit, where all current is carried by Cooper pairs. Unlike the finite-gap results shown in Figs. 8 and 9, parameters have been fine-tuned so as to make the current positive for all phase differences, φ_{sc}. Figure 12 also demonstrates an explicit dependence of the current on the initial conditions as a spread in curves obtained for different Floquet gauges [89], corresponding to different values of θ_R. This is indicated by a set of some 63 gray curves, corresponding to evenly spaced values of θ_R between 0 and 2π, which are averaged to obtain the blue curve. A similar spread will be obtained for the curves in Fig. 11 (not shown for clarity), whereas in Fig. 10, the driving amplitude is low enough that the results depend only on the phase difference, θ_d. This spread increases with driving amplitude and gives a rough indication of sensitivity of the long-time average of the Floquet time-evolved

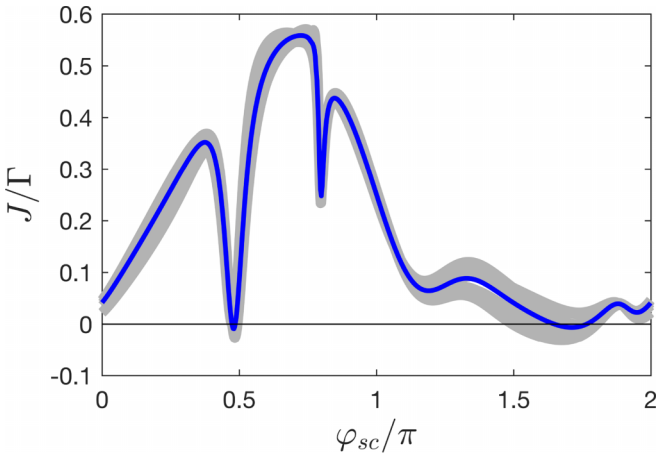

FIG. 12. Nearly rectified time-averaged current-phase relations in the infinite-gap limit for 63 evenly spaced values of $\theta_R \in [0, 2\pi]$ (gray curves) together with the corresponding θ_R-averaged (blue) curve. Parameters are chosen to be $\Omega = 2.1\Gamma$, $\theta_d = \pi/3$, $\varepsilon_d = 0.95\Gamma$, $t_d = 2\Gamma$, $A = 0.94\Gamma$, and $U = 0.045\Gamma$.

current on initial conditions, and thereby whether they can be expected to be valid also within a driven steady state.

2. Symmetries of the current

The time-dependent current and thereby its long-time average obeys a few basic symmetries, which are most easily revealed by reverting to the time-dependent infinite-gap Hamiltonian for the even sector obtained by replacing ε_d by $\varepsilon_d(t)$ in $\hat{H}_{e,\infty}$. The corresponding time-dependent infinite gap Hamiltonian, $\hat{H}(\varepsilon_d, \varphi_{sc}, \theta_L, \theta_R, t) = \hat{H}_{e,\infty}|_{\varepsilon_d \to \varepsilon_d(t)}$, and the current operator obey the transformation properties

$$\begin{aligned}
&\hat{\mathcal{I}}\hat{H}(\varphi_{sc}, \theta_L, \theta_R, U, \varepsilon_d, t)\hat{\mathcal{I}} = \hat{H}(-\varphi_{sc}, \theta_R, \theta_L, U, \varepsilon_d, t),\\
&\hat{\mathcal{C}}\hat{H}(\varphi_{sc}, \theta_L, \theta_R, U, \varepsilon_d, t)\hat{\mathcal{C}}\\
&\quad = \hat{H}(-\varphi_{sc}, \theta_L + \pi, \theta_R + \pi, U, -\varepsilon_d - U, t) + \delta\hat{H},
\end{aligned} \tag{A10}$$

and

$$\hat{\mathcal{I}}\hat{I}(\varphi_{sc})\hat{\mathcal{I}} = -\hat{I}(-\varphi_{sc}), \quad \hat{\mathcal{C}}\hat{I}(\varphi_{sc})\hat{\mathcal{C}} = -\hat{I}(-\varphi_{sc}), \tag{A11}$$

with orthogonal matrices given by

$$\hat{\mathcal{I}} = \begin{pmatrix} 1&0&0&0&0&0\\ 0&0&1&0&0&0\\ 0&1&0&0&0&0\\ 0&0&0&1&0&0\\ 0&0&0&0&0&-1\\ 0&0&0&0&-1&0 \end{pmatrix},$$

$$\hat{\mathcal{C}} = \begin{pmatrix} 0&0&0&1&0&0\\ 0&0&1&0&0&0\\ 0&1&0&0&0&0\\ 1&0&0&0&0&0\\ 0&0&0&0&0&-1\\ 0&0&0&0&-1&0 \end{pmatrix}, \tag{A12}$$

with $\hat{\mathcal{I}}$ corresponding to inversion, while $\hat{\mathcal{C}}$ is related to charge conjugation, but defined here without the complex conjugation operator. The correction term induced by $\hat{\mathcal{C}}$ has matrix elements

$$\delta\hat{H}_{ij} = \left[4\varepsilon_d + 2U + 2A\sum_{\alpha=L,R}\cos(\theta_\alpha + \Omega t)\right]\delta_{ij}, \tag{A13}$$

which merely shifts the diagonal terms, and amounts simply to a multiplicative phase factor between the transformation partner states. From the transformation properties (A10), one finds the transformation of a given solution to the time-dependent Schrödinger equation to be itself a solution with different parameters, namely,

$$\begin{aligned}
\hat{\mathcal{I}}|\Psi(\varphi_{sc}, \theta_L, \theta_R, U, \varepsilon_d, t)\rangle &= |\Psi(-\varphi_{sc}, \theta_R, \theta_L, U, \varepsilon_d, t)\rangle,\\
\hat{\mathcal{C}}|\Psi(\varphi_{sc}, \theta_L, \theta_R, U, \varepsilon_d, t)\rangle &= e^{-i[\Theta(t)-\Theta(0)]}|\Psi(-\varphi_{sc}, \theta_L\\
&\quad + \pi, \theta_R + \pi, U, -\varepsilon_d - U, t)\rangle,
\end{aligned} \tag{A14}$$

where the common time-dependent phase factor has been introduced as

$$\Theta(t) = 4(\varepsilon_d + U/2)t + 4(A/\Omega)\sum_{\alpha=L,R}\sin(\theta_\alpha + \Omega t). \tag{A15}$$

Together with the transformation properties of the current operator, this implies that

$$\begin{aligned}
&I(-\varphi_{sc}, \theta_R, \theta_L, U, \varepsilon_d, t)\\
&\quad = \langle\Psi(\varphi_{sc}, \theta_L, \theta_R, U, \varepsilon_d, t)|\hat{\mathcal{I}}\hat{I}(-\varphi_{sc})\hat{\mathcal{I}}\\
&\qquad \times |\Psi(\varphi_{sc}, \theta_L, \theta_R, U, \varepsilon_d, t)\rangle\\
&\quad = -I(\varphi_{sc}, \theta_L, \theta_R, U, \varepsilon_d, t)
\end{aligned} \tag{A16}$$

and

$$\begin{aligned}
&I(-\varphi_{sc}, \theta_L + \pi, \theta_R + \pi, U, -\varepsilon_d - U, t)\\
&\quad = \langle\Psi(\varphi_{sc}, \theta_L, \theta_R, U, \varepsilon_d, t)|\hat{\mathcal{C}}\hat{I}(-\varphi_{sc})\hat{\mathcal{C}}\\
&\qquad \times |\Psi(\varphi_{sc}, \theta_L, \theta_R, U, \varepsilon_d, t)\rangle\\
&\quad = -I(\varphi_{sc}, \theta_L, \theta_R, U, \varepsilon_d, t).
\end{aligned} \tag{A17}$$

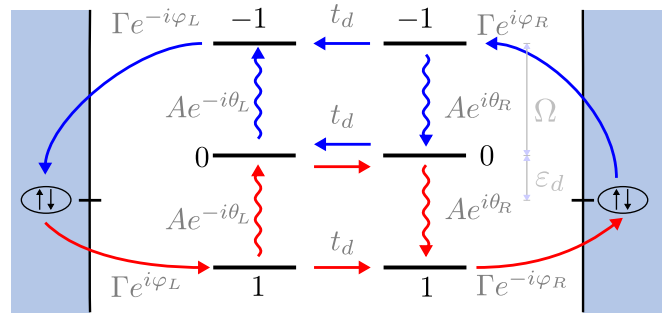

FIG. 13. Diagram illustrating the lowest order transport processes leading to anomalous Josephson current. The processes are similar to those illustrated in Fig. 2, but are shown here with two Floquet sidebands to each quantum dot level and with current carrying tunneling paths in both directions, which interfere destructively unless $\varepsilon_d \neq 0$, or with interactions included, $\varepsilon_d + U/2 \neq 0$.

From these instantaneous symmetries one may infer the symmetries (55) and (56) of the time-averaged currents,

$$J(\varphi_{sc}, \theta_d, U, \varepsilon_d) = -J(-\varphi_{sc}, \theta_d, U, -\varepsilon_d - U), \quad \text{(A18)}$$

$$= -J(-\varphi_{sc}, -\theta_d, U, \varepsilon_d), \quad \text{(A19)}$$

$$= J(\varphi_{sc}, -\theta_d, U, -\varepsilon_d - U), \quad \text{(A20)}$$

which are observed also in the noninteracting finite-gap numerical results shown in Figs. 8 and 9. The inversion symmetry relation (A19) alone dictates that the anomalous Josephson current must vanish at $\theta_d = \pi = 2\pi - \pi$, as observed in Fig. 11. The particle-hole symmetry relation (A18), and thereby (A20), holds only when the average phase of the two drives plays no role, i.e., when either the driving amplitude is sufficiently small or when all transients have been erased by relaxation via the quasiparticle continuum available for finite BCS gaps or weak tunneling to normal metals as modeled by Γ_m in the NESS Floquet-Keldysh Green's function method employed in the main text.

From these symmetries, the anomalous Josephson current at $\varphi_{sc} = 0$ is seen to satisfy the symmetries

$$J(0, \theta_d, U, \varepsilon_d) = -J(0, -\theta_d, U, \varepsilon_d) \quad \text{(A21)}$$

$$= -J(0, \theta_d, U, -\varepsilon_d - U). \quad \text{(A22)}$$

This implies that the anomalous Josephson current must vanish for quantum dots tuned to the particle-hole symmetric point, $\varepsilon_d = -U/2$. Within the Floquet picture, this vanishing of the anomalous Josephson current at the particle-hole symmetric point can be understood as a destructive interference between paths through respectively positive and negative Floquet sidebands. This is illustrated in Fig. 13, in which the blue and red paths need to be offset from particle-hole symmetry in order not to interfere destructively.

[1] Y. Makhlin, G. Schön, and A. Shnirman, Rev. Mod. Phys. **73**, 357 (2001).

[2] A. Blais, R.-S. Huang, A. Wallraff, S. M. Girvin, and R. J. Schoelkopf, Phys. Rev. A **69**, 062320 (2004).

[3] J. Clarke and F. K. Wilhelm, Nature (London) **453**, 1031 (2008).

[4] S. M. Girvin, in *Quantum Machines: Measurement and Control of Engineered Quantum Systems* (Oxford University Press, Oxford, England, UK, 2011).

[5] M. Kjaergaard, M. E. Schwartz, J. Braumüller, P. Krantz, J. I.-J. Wang, S. Gustavsson, and W. D. Oliver, Annu. Rev. Condens. Matter Phys. **11**, 369 (2020).

[6] I. O. Kulik, Pis'ma Zh. Eksp. Teor. Fiz. **50**, 799 (1966) [Sov. Phys. JETP **23**, 529 (1966)].

[7] H. Shiba and T. Soda, Prog. Theor. Phys. **41**, 25 (1969).

[8] C. W. J. Beenakker, Phys. Rev. Lett. **67**, 3836 (1991).

[9] L. I. Glazman and K. A. Matveev, Pis'ma Zh. Eksp. Teor. Fiz. **49**, 570 (1989) [JETP Lett. **49**, 659 (1989)].

[10] A. V. Rozhkov and D. P. Arovas, Phys. Rev. Lett. **82**, 2788 (1999).

[11] A. Martín-Rodero and A. Levy Yeyati, Adv. Phys. **60**, 899 (2011).

[12] V. Meden, J. Phys.: Condens. Matter **31**, 163001 (2019).

[13] J. A. van Dam, Y. V. Nazarov, E. P. A. M. Bakkers, S. De Franceschi, and L. P. Kouwenhoven, Nature (London) **442**, 667 (2006).

[14] R. Delagrange, R. Weil, A. Kasumov, M. Ferrier, H. Bouchiat, and R. Deblock, Phys. Rev. B **93**, 195437 (2016).

[15] D. J. van Woerkom, A. Proutski, B. van Heck, D. Bouman, J. I. Väyrynen, L. I. Glazman, P. Krogstrup, J. Nygård, L. P. Kouwenhoven, and A. Geresdi, Nat. Phys. **13**, 876 (2017).

[16] D. Bouman, R. J. J. van Gulik, G. Steffensen, D. Pataki, P. Boross, P. Krogstrup, J. Nygård, J. Paaske, A. Pályi, and A. Geresdi, Phys. Rev. B **102**, 220505(R) (2020).

[17] T. W. Larsen, K. D. Petersson, F. Kuemmeth, T. S. Jespersen, P. Krogstrup, J. Nygård, and C. M. Marcus, Phys. Rev. Lett. **115**, 127001 (2015).

[18] L. Casparis, T. W. Larsen, M. S. Olsen, F. Kuemmeth, P. Krogstrup, J. Nygård, K. D. Petersson, and C. M. Marcus, Phys. Rev. Lett. **116**, 150505 (2016).

[19] L. Casparis, M. R. Connolly, M. Kjaergaard, N. J. Pearson, A. Kringhøj, T. W. Larsen, F. Kuemmeth, T. Wang, C. Thomas, S. Gronin, G. C. Gardner, M. J. Manfra, C. M. Marcus, and K. D. Petersson, Nat. Nanotechnol. **13**, 915 (2018).

[20] J. Koch, T. M. Yu, J. Gambetta, A. A. Houck, D. I. Schuster, J. Majer, A. Blais, M. H. Devoret, S. M. Girvin, and R. J. Schoelkopf, Phys. Rev. A **76**, 042319 (2007).

[21] L. DiCarlo, J. M. Chow, J. M. Gambetta, L. S. Bishop, B. R. Johnson, D. I. Schuster, J. Majer, A. Blais, L. Frunzio, S. M. Girvin, and R. J. Schoelkopf, Nature (London) **460**, 240 (2009).

[22] J. Kelly, R. Barends, A. G. Fowler, A. Megrant, E. Jeffrey, T. C. White, D. Sank, J. Y. Mutus, B. Campbell, Y. Chen, Z. Chen, B. Chiaro, A. Dunsworth, I.-C. Hoi, C. Neill, P. J. J. O'Malley, C. Quintana, P. Roushan, A. Vainsencher, J. Wenner *et al.*, Nature (London) **519**, 66 (2015).

[23] A. Kandala, A. Mezzacapo, K. Temme, M. Takita, M. Brink, J. M. Chow, and J. M. Gambetta, Nature (London) **549**, 242 (2017).

[24] C. Neill, P. Roushan, K. Kechedzhi, S. Boixo, S. V. Isakov, V. Smelyanskiy, A. Megrant, B. Chiaro, A. Dunsworth, K. Arya, R. Barends, B. Burkett, Y. Chen, Z. Chen, A. Fowler, B. Foxen, M. Giustina, R. Graff, E. Jeffrey, T. Huang *et al.*, Science **360**, 195 (2018).

[25] A. Zazunov, R. Egger, T. Jonckheere, and T. Martin, Phys. Rev. Lett. **103**, 147004 (2009).

[26] V. B. Geshkenbein and A. I. Larkin, Pis'ma Zh. Eksp. Teor. Fiz. **43**, 306 (1986) [Sov. Phys. JETP **43**, 395 (1986)].

[27] A. Buzdin and A. E. Koshelev, Phys. Rev. B **67**, 220504(R) (2003).

[28] A. A. Reynoso, G. Usaj, C. A. Balseiro, D. Feinberg, and M. Avignon, Phys. Rev. Lett. **101**, 107001 (2008).

[29] Y. Tanaka, T. Yokoyama, and N. Nagaosa, Phys. Rev. Lett. **103**, 107002 (2009).

[30] J.-F. Liu and K. S. Chan, Phys. Rev. B **82**, 184533 (2010).

[31] E. Goldobin, D. Koelle, R. Kleiner, and R. G. Mints, Phys. Rev. Lett. **107**, 227001 (2011).

[32] A. Brunetti, A. Zazunov, A. Kundu, and R. Egger, Phys. Rev. B **88**, 144515 (2013).

[33] M. Alidoust and J. Linder, Phys. Rev. B **87**, 060503(R) (2013).

[34] T. Yokoyama, M. Eto, and Y. V. Nazarov, Phys. Rev. B **89**, 195407 (2014).

[35] G. Campagnano, P. Lucignano, D. Giuliano, and A. Tagliacozzo, J. Phys.: Condens. Matter **27**, 205301 (2015).

[36] F. S. Bergeret and I. V. Tokatly, Europhys. Lett. **110**, 57005 (2015).

[37] F. Dolcini, M. Houzet, and J. S. Meyer, Phys. Rev. B **92**, 035428 (2015).

[38] M. Alidoust, Phys. Rev. B **101**, 155123 (2020).

[39] H. Sickinger, A. Lipman, M. Weides, R. G. Mints, H. Kohlstedt, D. Koelle, R. Kleiner, and E. Goldobin, Phys. Rev. Lett. **109**, 107002 (2012).

[40] D. B. Szombati, S. Nadj-Perge, D. Car, S. R. Plissard, E. P. A. M. Bakkers, and L. P. Kouwenhoven, Nat. Phys. **12**, 568 (2016).

[41] Z. Su, A. B. Tacla, M. Hocevar, D. Car, S. R. Plissard, E. P. A. M. Bakkers, A. J. Daley, D. Pekker, and S. M. Frolov, Nat. Commun. **8**, 585 (2017).

[42] J. C. Estrada Saldaña, A. Vekris, G. Steffensen, R. Žitko, P. Krogstrup, J. Paaske, K. Grove-Rasmussen, and J. Nygård, Phys. Rev. Lett. **121**, 257701 (2018).

[43] J. C. Estrada Saldaña, A. Vekris, R. Žitko, G. Steffensen, P. Krogstrup, J. Paaske, K. Grove-Rasmussen, and J. Nygård, Phys. Rev. B **102**, 195143 (2020).

[44] J. Bauer, A. Oguri, and A. C. Hewson, J. Phys.: Condens. Matter **19**, 486211 (2007).

[45] T. Meng, S. Florens, and P. Simon, Phys. Rev. B **79**, 224521 (2009).

[46] S. Droste, S. Andergassen, and J. Splettstoesser, J. Phys.: Condens. Matter **24**, 415301 (2012).

[47] G. Kiršanskas, M. Goldstein, K. Flensberg, L. I. Glazman, and J. Paaske, Phys. Rev. B **92**, 235422 (2015).

[48] A. Kadlecová, M. Žonda, V. Pokorný, and T. Novotný, Phys. Rev. Appl. **11**, 044094 (2019).

[49] V. Pokorný, M. Žonda, G. Loukeris, and T. Novotný, JPS Conf. Proc. **30**, 011002 (2020).

[50] A. Haller, M.Sc. thesis, University of Copenhagen, 2014, https://www.nbi.ku.dk/english/theses/masters-theses/anika-haller/.

[51] C. Hermansen, A. L. Yeyati, and J. Paaske, Phys. Rev. B **105**, 054503 (2022).

[52] P. D. Kurilovich, V. D. Kurilovich, V. Fatemi, M. H. Devoret, and L. I. Glazman, Phys. Rev. B **104**, 174517 (2021).

[53] P. K. Tien and J. P. Gordon, Phys. Rev. **129**, 647 (1963).

[54] M. Grifoni and P. Hänggi, Phys. Rep. **304**, 229 (1998).

[55] G. Platero and R. Aguado, Phys. Rep. **395**, 1 (2004).

[56] F. S. Bergeret, P. Virtanen, T. T. Heikkilä, and J. C. Cuevas, Phys. Rev. Lett. **105**, 117001 (2010).

[57] F. S. Bergeret, P. Virtanen, A. Ozaeta, T. T. Heikkilä, and J. C. Cuevas, Phys. Rev. B **84**, 054504 (2011).

[58] F. Kos, S. E. Nigg, and L. I. Glazman, Phys. Rev. B **87**, 174521 (2013).

[59] L. Bretheau, Ç. Ö. Girit, M. Houzet, H. Pothier, D. Esteve, and C. Urbina, Phys. Rev. B **90**, 134506 (2014).

[60] D. G. Olivares, A. L. Yeyati, L. Bretheau, Ç. Ö. Girit, H. Pothier, and C. Urbina, Phys. Rev. B **89**, 104504 (2014).

[61] B. Venitucci, D. Feinberg, R. Mélin, and B. Douçot, Phys. Rev. B **97**, 195423 (2018).

[62] S. A. González, L. Melischek, O. Peters, K. Flensberg, K. J. Franke, and F. von Oppen, Phys. Rev. B **102**, 045413 (2020).

[63] B. Baran, R. Taranko, and T. Domański, Sci. Rep. **11**, 11138 (2021).

[64] L. Bretheau, C. Ö. Girit, H. Pothier, D. Esteve, and C. Urbina, Nature (London) **499**, 312 (2013).

[65] C. Janvier, L. Tosi, L. Bretheau, Ç. Ö. Girit, M. Stern, P. Bertet, P. Joyez, D. Vion, D. Esteve, M. F. Goffman, H. Pothier, and C. Urbina, Science **349**, 1199 (2015).

[66] A. Blais, A. L. Grimsmo, S. M. Girvin, and A. Wallraff, Rev. Mod. Phys. **93**, 025005 (2021).

[67] O. Peters, N. Bogdanoff, S. Acero González, L. Melischek, J. R. Simon, G. Reecht, C. B. Winkelmann, F. von Oppen, and K. J. Franke, Nat. Phys. **16**, 1222 (2020).

[68] F. J. M. Cañadas, C. Metzger, S. Park, L. Tosi, P. Krogstrup, J. Nygård, M. F. Goffman, C. Urbina, H. Pothier, and A. L. Yeyati, Phys. Rev. Lett. **128**, 197702 (2022).

[69] V. Fatemi, P. D. Kurilovich, M. Hays, D. Bouman, T. Connolly, S. Diamond, N. E. Frattini, V. D. Kurilovich, P. Krogstrup, J. Nygard, A. Geresdi, L. I. Glazman, and M. H. Devoret, Phys. Rev. Lett. **129**, 227701 (2022).

[70] A. Soori and M. Sivakumar, J. Phys.: Condens. Matter **32**, 365304 (2020).

[71] L. V. Keldysh, Zh. Eksp. Teor. Fiz **47**, 1018 (1964).

[72] J. Rammer and H. Smith, Rev. Mod. Phys. **58**, 323 (1986).

[73] H. Haug and A.-P. Jauho, *Quantum Kinetics in Transport and Optics of Semiconductors | SpringerLink* (Springer, Berlin, Heidelberg, 2008).

[74] F. H. M. Faisal, Comput. Phys. Rep. **9**, 57 (1989).

[75] N. Tsuji, T. Oka, and H. Aoki, Phys. Rev. B **78**, 235124 (2008).

[76] V. Ambegaokar and A. Baratoff, Phys. Rev. Lett. **10**, 486 (1963).

[77] M. Hays, G. de Lange, K. Serniak, D. J. van Woerkom, D. Bouman, P. Krogstrup, J. Nygård, A. Geresdi, and M. H. Devoret, Phys. Rev. Lett. **121**, 047001 (2018).

[78] M. Hays, V. Fatemi, K. Serniak, D. Bouman, S. Diamond, G. de Lange, P. Krogstrup, J. Nygård, A. Geresdi, and M. H. Devoret, Nat. Phys. **16**, 1103 (2020).

[79] M. Hays, V. Fatemi, D. Bouman, J. Cerrillo, S. Diamond, K. Serniak, T. Connolly, P. Krogstrup, J. Nygård, A. L. Yeyati, A. Geresdi, and M. H. Devoret, Science **373**, 430 (2021).

[80] R.-P. Riwar and J. Splettstoesser, Phys. Rev. B **82**, 205308 (2010).

[81] F. Ando, Y. Miyasaka, T. Li, J. Ishizuka, T. Arakawa, Y. Shiota, T. Moriyama, Y. Yanase, and T. Ono, Nature (London) **584**, 373 (2020).

[82] C. Baumgartner, L. Fuchs, A. Costa, S. Reinhardt, S. Gronin, G. C. Gardner, T. Lindemann, M. J. Manfra, P. E. Faria Junior, D. Kochan, J. Fabian, N. Paradiso, and C. Strunk, Nat. Nanotechnol. **17**, 39 (2022).

[83] H. Wu, Y. Wang, Y. Xu, P. K. Sivakumar, C. Pasco, U. Filippozzi, S. S. P. Parkin, Y.-J. Zeng, T. McQueen, and M. N. Ali, Nature (London) **604**, 653 (2022).

[84] R. S. Souto, M. Leijnse, and C. Schrade, Phys. Rev. Lett. **129**, 267702 (2022).

[85] A. Soori, arXiv:2206.07014.

[86] H. Sambe, Phys. Rev. A **7**, 2203 (1973).

[87] J. H. Shirley, Phys. Rev. **138**, B979 (1965).

[88] A. Eckardt and E. Anisimovas, New J. Phys. **17**, 093039 (2015).

[89] M. Bukov, L. D'Alessio, and A. Polkovnikov, Adv. Phys. **64**, 139 (2015).